NOVEL POLARIZATION-DIVERSITY DEVICES ON A SILICON-ON-INSULATOR PLATFORM

GUAN HANG

NATIONAL UNIVERSITY OF SINGAPORE

2014

NOVEL POLARIZATION-DIVERSITY DEVICES ON A SILICON-ON-INSULATOR PLATFORM

GUAN HANG

(B. Eng., University of Electronic Science and Technology of China)

A THESIS SUBMITTED

FOR THE DEGREE OF MASTER OF ENGINEERING

DEPARTMENT OF ELECTRICAL AND COMPUTER ENGINEERING

NATIONAL UNIVERSITY OF SINGAPORE

2014

DECLARATION

I hereby declare that this thesis is my original work and it has been written by me in its entirety. I have duly acknowledged all the sources of information, which have been used in the thesis. This thesis has not been submitted for any degree in any university previously.

GUAN, HANG

JULY 2014

ACKNOWLEDGMENTS

My year-and-a-half study at the National University of Singapore has been a wonderful and fulfilling experience. Besides gaining knowledge, I came to know many great people, without whom I would not have been able to finish my study.

I am mostly indebted to my advisor Prof. Michael Hochberg for his guidance and support throughout the years. His far-reaching vision in both academic and industrial sides is highly appreciated. I would also like to thank my co-supervisors, Dr. Patrick Guo-Qiang Lo and Dr. Qing Fang of the Institute of Microelectronics. They provided me with endless support and great suggestions on my thesis project.

Special thanks go to the entire Nanophotonics Group at both National University of Singapore and University of Delaware. They are a wonderful group of people as both colleagues and friends to whom I cannot be more grateful. My first thanks go to Prof. Tom Baehr-Jones for leading me into the nanophotonics world and offering me great help in graduate work. I have enjoyed working with Ari Novack, Matthew Streshinsky, Ruizhi Shi, Yangjin Ma, Charlie Lin, Dr. Thomas Ang, Dr. Ran Ding, Dr. Yang Liu, Yi Zhang and Shuyu Yang.

Thanks also go to staff members at the Nanophotonics Group of the Institute of Microelectronics, particularly Dr. Andy Eu-Jin Lim, Dr. Junfeng Song, Edward Koh Sing Chen, Chen Kok Kiong and many others. Their help has been extremely valuable. I would also like to express my sincere gratitude to Prof. Changyuan Yu and all the members in the Photonic System Research Group.

Last but not least, I would like to thank my parents for their constant love and encouragement. They have sacrificed a lot in their lives so that I wouldn't have to sacrifice anything in mine. Thanks for always being there for me.

TABLE OF CONTENTS

ABSTRACT

Silicon photonics built on a silicon-on-insulator (SOI) platform has received much attention in recent years due to its compatibility with complementary metal-oxide-semiconductor (CMOS) technology, which makes the mass production of photonics devices cost-effective. The intrinsic high-index contrast property of SOI allows for photonics with very small footprint, which is highly desirable for system integration. However, this property results in high polarization dependence for silicon photonic devices. To solve this problem, polarization diversity circuits have been proposed in the literature.

In this thesis, four different types of novel polarization diversity devices were explored and demonstrated on a 220 nm SOI platform. The thesis contributes significantly to further improving the polarization transparency of silicon photonic circuits. This will enhance the viability of silicon photonics for commercialization.

First, a novel polarization splitter-rotator based on a double-etched directional coupler was demonstrated on a 220 nm SOI platform using a 248 nm deep ultraviolet lithography. The polarization splitter-rotator has a very compact footprint (with a device length of 27 μm). In addition, the fabricated polarization splitter-rotator yields a TM-to-TE polarization conversion loss better than 0.5 dB and TE insertion loss better than 0.3 dB, with an ultra-low crosstalk (- 20 dB) in the wavelength regime 1540-1570 nm.

Second, a novel polarization splitter-rotator based on a Mach-Zehnder mode converter was demonstrated on a 220 nm SOI platform using a 248 nm deep ultraviolet lithography. To the best of our knowledge, this is the first polarization splitter-rotator that is designed for the O-band on a SOI platform. The fabricated

polarization splitter-rotator yields a polarization conversion loss better than 2 dB and TE insertion loss better than 0.5 dB, with an ultra-low crosstalk (- 20 dB) in the wavelength regime 1290-1330 nm.

Third, a bi-wavelength polarization splitter-rotator, which operates at both O-band and C-band, was demonstrated on a 220 nm SOI platform using a 248 nm deep ultraviolet lithography. To the best of our knowledge, this is the world's first work that proposed and discussed the design of a bi-wavelength polarization splitter-rotator. Our proposed polarization splitter-rotator has a simulated insertion loss of 0.9 dB at 1310 nm and 1 dB at 1550 nm. We believe that combining this bi-wavelength polarization splitter-rotator with a wideband edge coupler to offer a high-efficiency edge-coupling-based light duplexing solution.

Last but not least, a polarization rotator was demonstrated on a 220 nm SOI platform. The rotator has a compact footprint (with a device length of 15.3 μm), a simulated polarization conversion loss lower than 0.2 dB and a polarization extinction ratio larger than 25 dB over a wavelength range of 80 nm around 1550 nm. This was the first time that evolutionary optimization method, like particle swarm optimization method, had been used into the design of polarization rotator.

LIST OF TABLES

LIST OF FIGURES

CHAPTER 1
INTRODUCTION

1.1 Silicon photonics for on-chip optical interconnects

The continuing scaling of transistors has significantly boosted the processing power of computers. Consequently, microprocessors have evolved from single-core architectures to present day multi-core architectures. It is expected that in the near future, microprocessors will incorporate hundreds or even thousands of cores [1]. In order to fully leverage multi-core computing power, there is a need to offer an inter-core communication technology so that data and control messages could be exchanged among cores efficiently. However, traditional interconnects using metal wires for on-chip communication cannot keep pace with the growth of this need, and are becoming the bottleneck of the system [2, 3]. Traditional metal interconnects cannot meet the bandwidth, power consumption and latency requirements of future on-chip communication. A recent on-chip electrical network, designed for an 80-core interconnection [4] and fabricated in a 65 nm technology and operated at 5 GHz, consumed 28% of the total operating power [1]. This clearly limits the power budget for the microprocessor. Also, this on-chip electrical network introduced a five-clock cycle latency, which limits the throughput of the system [4].

Silicon photonics has been proposed as a very promising technology for next-generation on-chip communication for a number of reasons:

First, the high index-contrast between the silicon core and the cladding material (SiO_2, air, etc.) allows the design of very compact photonic systems. This is a very important aspect since the real estate of the on-chip system is one of the

biggest concerns. The optical mode can be mostly confined in the silicon core and allows very tight bends with sub-micrometer radii [5, 6]. Currently, most silicon photonic components, including modulators, detectors, switches and almost all the passive components (Y-junctions, crossings, etc.), are in the range of few tens of micrometers [7-13], which is more than one order of magnitude smaller than silica-based devices that are widely used in telecommunication networks [14].

Second, with the dramatic scaling in size, the power consumption of the silicon photonic devices is also significantly reduced. For instance, the first generation 100 Gbps C Form Factor Pluggable (CFP – a standardized pluggable transceiver that supports 100 Gbps Ethernet) transceivers consume 20-24 watts, but a silicon photonic solution can be less than 3.5 watts. Not only is this far less than 100 Gbps solutions, silicon is also 70% less than 10 Gbps solutions [15].

Third, silicon photonics could provide a wide variety of optical functionalities. A huge advantage of optical communication is the ability to provide parallel channels over the same optical fiber using different wavelengths of light. With wavelength-division multiplexing technology, tens of or even hundreds of channels could be transmitted using a single strand of optical fiber. Fiber is cheap compared to copper cables. Basically, the components in silicon photonic interconnects mimic those found in traditional wavelength-division multiplexed optical communications systems [1]. The typical link is composed of a light source, modulators, multiplexers, de-multiplexers, detectors and waveguides with attendant routing. Except for the light source, all the other components mentioned above have been demonstrated on a silicon-on-insulator platform. Hybrid lasers incorporating III-V quantum wells onto silicon have been demonstrated in literature [16]. Other gain media such as erbium and germanium have also been widely explored [17, 18]. Modulators such as those based on

microring resonators and Mach-Zehnder modulators have been reported with the highest speed up to 50 Gbps [19, 20]. Photodetectors based on various materials such as germanium [10, 21], silicide [22], or III-V materials [23] have been shown in the literature as well. Passive components, including switching and routing networks [13, 24], polarization-diversity devices [25], Y-junctions [11], waveguide crossings [12, 26], and etc. have also been demonstrated in the literature.

Last but not least, silicon photonics could be fabricated using complementary metal-oxide-semiconductor (CMOS)-compatible processes and has the potential to be integrated on the same chip as the microelectronics. This offers a great advantage compared with other hybrid processes or chip-to-chip bonding schemes, and can reduce the packaging complexity as well as improve the system performance [27]. More importantly, by leveraging the mature microelectronics manufacture infrastructure and process, the cost of the silicon photonic circuits could be extremely reduced. There is lots of on-going research towards a full integration of both photonic and electronic circuits on a single chip [28-30]. It is worth mentioning that there are already commercial products that integrate both active silicon photonic components and silicon electrical driving circuits [30].

1.2 Polarization-diversity devices for silicon photonic integrated circuits

Polarization-diversity devices, including polarization rotators, polarization beam splitters, polarization splitter-rotators, and polarization controllers and so on and so forth are very useful for many applications.

First, polarization-diversity components could be used to eliminate the polarization sensitivity (or polarization dependence) of photonic integrated circuits, which are based on silicon-on-insulator waveguides. Due to the high index-contrast between the silicon core and the cladding (SiO_2 or air), silicon-on-insulator waveguides usually have a very large birefringence. For the silicon-on-insulator ridge waveguides, the birefringence is on the order of 10^{-3}-10^{-5}, while the birefringence of silicon-on-insulator nanowire could be several orders of magnitude higher [31]. This birefringence introduces significant polarization dependence to silicon-on-insulator photonic integrated circuits [32]. For typical fiber optical communication applications, the light coupled from an optical fiber usually has a random polarization state. Because in most cases, we use single mode fibers, not polarization-maintaining fibers, and single mode fibers do not maintain polarization states. Consequently, the uncertainty of polarization state will degrade the signal-to-noise ratio after the light goes through polarization-sensitive photonic integrated circuits. Therefore, polarization-insensitive photonic integrated circuits are highly desired.

It is usually very hard to achieve non-birefringent silicon-on-insulator nanowires experimentally using the conventional way, which is to design the dimensions of the nanowire such that the refractive indices of the TE mode and TM mode are exactly the same [32]. The reason is that optical lithography will introduce a very large uncertainty in the dimensions, and this will break the above condition easily. The general principle to eliminate polarization sensitivity is the so-called polarization transparent circuits [33], which is described as follows: a polarization beam splitter first separates the input light. Then, one of the polarized beams (usually the TM mode) is converted into the orthogonal mode (TE mode) with a polarization rotator, and the other polarized beam

remains the same. After that, the two beams with the same polarization state (both of them are TE mode now) enter two identical photonic integrated circuits separately. Then, one of the two outputs is converted back to its original polarization state (TM mode) using a second polarization rotator. Finally, the two beams are combined with a polarization beam combiner. As can be seen from the above description, polarization-diversity components play an important role in implementing polarization-insensitive circuits.

Second, polarization-diversity components could be used to implement polarization-division multiplexing technology to double the transmission capability of an optical link. In order to extend the capacity of an optical transmission link, various kinds of multiplexing technologies have been exploited, including wavelength-division multiplexing, polarization-division multiplexing, phase-division multiplexing, and mode-division multiplexing. Among all these multiplexing technologies, polarization-division multiplexing is considered to be a suitable and cost-effective way to double the capacity for photonic network-on-chip, because planar optical waveguides could maintain the polarization state, which is crucial to the success of polarization-division multiplexing [34]. In addition, polarization-division multiplexing could work in conjunction with many other multiplexing schemes like mode-division multiplexing [35, 36] to further expand the transmission capability of an optical link.

Last but not least, polarization-diversity components could be used in many other applications. For example, polarization-diversity components have been used for long-haul coherent optical communications [37]. More recently, in the area of quantum optics, polarization-diversity component based polarization-handling technology has been proven to be very useful [38], too.

1.3 Focus and contributions of this dissertation

This thesis is comprised of four different polarization-diversified devices, including a polarization splitter-rotator based on a double-etched directional coupler, a polarization splitter-rotator based on a Mach-Zehnder mode converter, a bi-wavelength polarization splitter-rotator and an ultra-compact polarization rotator optimized using particle swarm optimization. All of these four devices are based on the works that I have done during the past year and a half. And the first two of them have been fabricated using Optoelectronic Systems In Silicon (OpSIS) Multi-Project Wafer (MPW) Shuttle runs [39]. The last two are simulation works, which have not got a chance to fabricate. All in all, these works have contributed three peer-reviewed journal papers [40-42] and form the core of my project. The title of my project is "Novel polarization-diversified devices and circuits on a silicon-on-insulator platform" and I would like to take advantage of this opportunity to summarize and introduce the works that I have done in this project.

(a) Polarization splitter-rotator based on a double-etched directional coupler

Using a double-etched directional coupler, we demonstrate a highly efficient polarization splitter-rotator, which is fabricated using 248 nm deep ultraviolet lithography on a silicon-on-insulator substrate. The polarization splitter-rotator has a very compact footprint (with a device length of 27 μm). In addition, the fabricated polarization splitter-rotator yields a TM-to-TE polarization conversion loss better than 0.5 dB and TE insertion loss better than 0.3 dB, with an ultra-low

crosstalk (- 20 dB) in the wavelength regime 1540-1570 nm. In chapter 2, we first discuss the motivation and the design of the novel polarization splitter-rotator. We then present the simulation, fabrication, and the testing results of the polarization splitter-rotator. At the end we discuss the fabrication tolerance, showing that this device is potentially suitable for industrial application. This research work has been published in [40].

(b) Polarization splitter-rotator based on a Mach-Zehnder mode converter

Using a 248 nm deep ultraviolet lithography, we demonstrate the first polarization splitter-rotator at 1310 nm built on a silicon-on-insulator platform. The polarization splitter-rotator is constructed with a directional coupler, which works as a polarization beam splitter, a bi-level taper mode converter, and an asymmetric Mach-Zehnder mode converter. In addition, the fabricated polarization splitter-rotator yields a polarization conversion loss better than 2 dB and TE insertion loss better than 0.5 dB, with an ultra-low crosstalk (- 20 dB) in the wavelength regime 1290-1330 nm. In chapter 3, we first discuss the motivation and the design of the polarization splitter-rotator. We then elaborate on the simulation, fabrication, and testing results of the polarization splitter-rotator. At the end we discuss the fabrication tolerance (robustness) of this device. This research work has been published in [41].

(c) Bi-wavelength polarization splitter-rotator

In chapter 4, we present the design of a polarization splitter-rotator that operates at both 1310 nm and 1550 nm. Our proposed polarization splitter-rotator has a

simulated insertion loss of 0.9 dB at 1310 nm and 1 dB at 1550 nm. In this part, we will mainly discuss the design methodology of a bi-wavelength polarization splitter-rotator by utilizing a structure comprising a bi-level taper and an asymmetric directional coupler. At the end we discuss the potential of combining this bi-wavelength polarization splitter-rotator with a wideband edge coupler to offer a high-efficiency edge-coupling-based light duplexing solution.

(d) Ultra-compact and high-efficiency polarization rotator

We proposed a polarization rotator, which has a compact footprint (with a device length of 15.3 μm), a simulated polarization conversion loss lower than 0.2 dB and a polarization extinction ratio larger than 25 dB over a wavelength range of 80 nm around 1550 nm. We will mainly discuss the optimization using the particle swarm optimization method. And we also discuss the design of an ultra-short bi-level mode converter and a bent-taper-shaped mode converter. This research work has been published in [42] and will be described in chapter 5.

1.4 Organization of this Dissertation

This report is organized as follows. The first chapter gives an introduction, followed by an overview of the focus and significant contributions of this research work. Subsequently, we elaborate on the completed research work, which is outlined earlier in section 1.3, in chapter 2 to chapter 5. Finally, in chapter 6, we summarize and conclude all the major contributions of this thesis as well as suggesting research directions for our future work.

CHAPTER 2
POLARIZATION SPLITTER-ROTATOR BASED ON A DOUBLE-ETCHED DIRECTIONAL COUPLER

As we discussed in chapter 1, silicon photonics has received much attention in the last decade. The main reason is that it can be fabricated in a complementary metal-oxide-semiconductor (CMOS) process, which can leverage the existing manufacturing infrastructure in support of low cost photonic integration [43-44]. One of the main characteristics of the silicon-on-insulator process based silicon photonic system is the high refractive index contrast between the silicon core and the cladding. This property is highly desirable because the mode of light is mainly confined in the waveguide and this could make photonic devices extremely small [45-46]. However, this property leads to some problems too. One of the main problems is that it causes severe polarization dependence, which means that most photonic devices built on silicon-on-insulator platform may work well in one particular polarization state, but could experience obvious performance degradation in the orthogonal polarization state.

To address this problem, one most commonly adopted way is to implement polarization-diversity circuits [47-49] to separate the random polarization state into two orthogonal polarization states when light is coupled from optical fibers into the chips. There are mainly two kinds of devices, which can cater to this need [50]. One category is based on two-dimensional grating couplers [51] (or so-called polarization splitter grating couplers), and the other category is based on polarization splitter-rotators [52-53]. We will only look into the polarization splitter-rotators in this thesis.

In this chapter, we demonstrate a novel polarization splitter-rotator, which is based on a double-etched directional coupler. The device has a very compact footprint (27 μm in length), and used silicon dioxide as a symmetric cladding. More importantly, this device has a 0.3 dB TE-to-TE insertion loss and a 0.5 dB TM-to-TE polarization conversion loss over a bandwidth of 30 nm centered at 1550 nm.

2.1 Basics of polarization splitter-rotator

The functionality of a polarization splitter-rotator is to separate two orthogonal polarization states and then rotate one polarization state into the other. Thus, at the two outputs of the polarization splitter-rotator, you will have only one fixed polarization state, not a random polarization state, which could be considered as a mixture of two orthogonal polarization states. This is a very important step before letting the light goes through the subsequent photonic integrated circuits, because most photonics devices that are built on a silicon-on-insulator platform have very large polarization dependent losses.

There are various kinds of polarization splitter-rotators. In this chapter, we will mainly focus on coupling-based polarization splitter-rotators, and in chapter 3, we will discuss another mode-evolution-based polarization splitter-rotators. Polarization splitter-rotators based on symmetrical directional couplers have been demonstrated in the literature [50, 54, 55]. However, these demonstrations are not ideal, because they are patterned using electron beam lithography (EBL) with air as top cladding. Although this lack of top cladding could break the vertical symmetry of the silicon core and make polarization rotation easier to achieve, this raises another problem - it is not compatible with metal back-end-

of-line process. In order to make polarization splitter-rotators compatible with complementary metal-oxide-semiconductor process, we have to use a silicon dioxide as a top cladding, not air. Polarization rotators using silicon dioxide as cladding were recently proposed in the literature [56-57] on a 220 nm silicon-on-insulator platform using a 193 nm deep ultraviolet lithography. However, the worst-case insertion loss of the proposed device is still very high (2.5 dB).

2.2 Design of polarization splitter-rotator based on a double-etched directional coupler

The schematic of our proposed polarization splitter-rotator is shown in Figure 2.1. There are several key parameters that require special attention. First, this device is fabricated on a 220 nm silicon-on-insulator platform. Thus, the top silicon thickness H_1 = 220 nm and a partially-etched silicon thickness H_2 = 90 nm. Width parameters (W_1, W_2, W_3, and W_g) are also very important because they define the cross section shape of the double-etched directional coupler. Finally, we should pay attention to the length parameter L_5, because it controls the coupling length.

In order to make this polarization splitter-rotator work, we need to make sure two things. The first thing is that we need to make sure that the refractive index of the TM_0 mode in the ridge waveguide is close enough to the refractive index of the TE_0 mode in the double-etched waveguide. The second thing is we need to make sure the refractive index of the TE_0 mode in the ridge waveguide is quite different to the refractive index of the TE_0 mode in the double-etched waveguide. The working principle of this device is described as follows.

Both the TE_0 mode and the TM_0 mode will be launched into the ridge waveguide on the bottom left in Figure 2.1. In case of inputting TM_0 mode, the light will be gradually coupled to the double-etched waveguide as it propagates in the ridge waveguide. And more importantly, the TM_0 mode will be converted into the TE_0 mode and come out from the cross port. In order to achieve an efficient cross-polarization coupling, we need to use a double-etched waveguide to break the symmetry of the surrounding [50, 56-59]. On the other hand, if we input TE_0 mode into the input port, the light will keep propagating along the ridge waveguide and comes out from the through port.

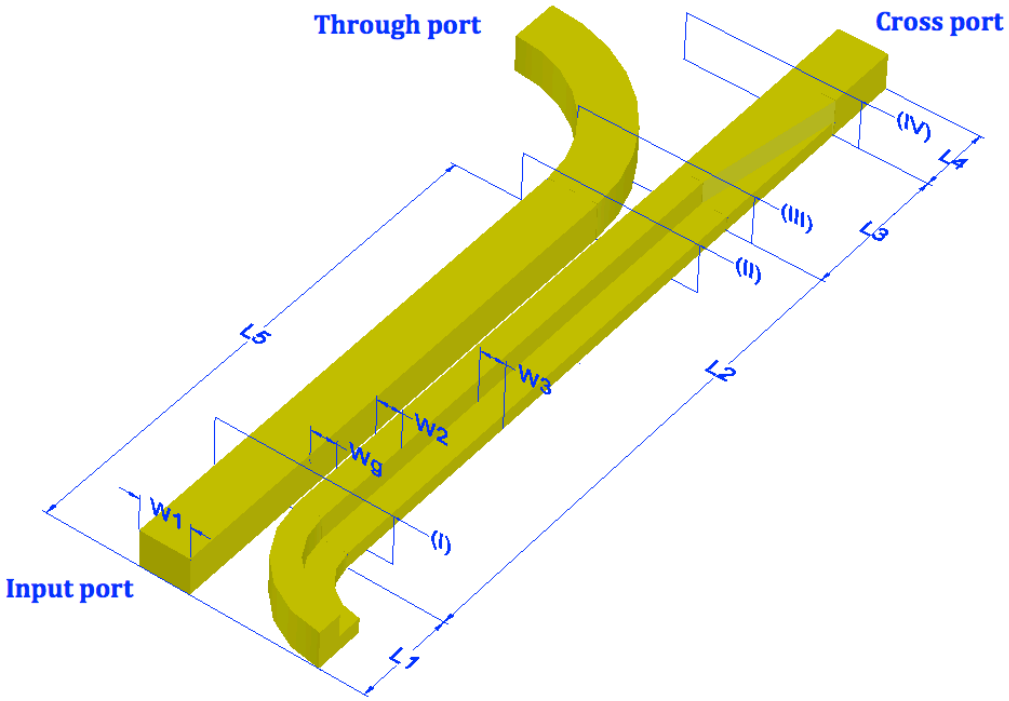

Figure 2.1. Schematic structure of the proposed PSR with significant geometric parameters noted.

After optimization, we fixed the values of the parameters: W_1 = 480 nm, W_2 = 190 nm, W_3 = 200 nm, W_g = 200 nm, L_1 =5 μm, L_2= 19 μm, L_3 =3 μm, L_4=1 μm, L_5 = 21 μm. The device could be seen as three sections. The first section is the input

section. A bend is introduced in the double-etched waveguide side, which is used to make an adiabatic transition of the refractive index and therefore minimize the backscattering. The second section is the coupling section, where the input TM_0 mode will be completely coupled to the other side. The last section is the output section. A bend is connected on the ridge waveguide side, which is used to isolate these two waveguides and prevent further coupling at the through port. And the double-etched stair-shaped waveguide is gradually converted to a ridge waveguide at the cross port.

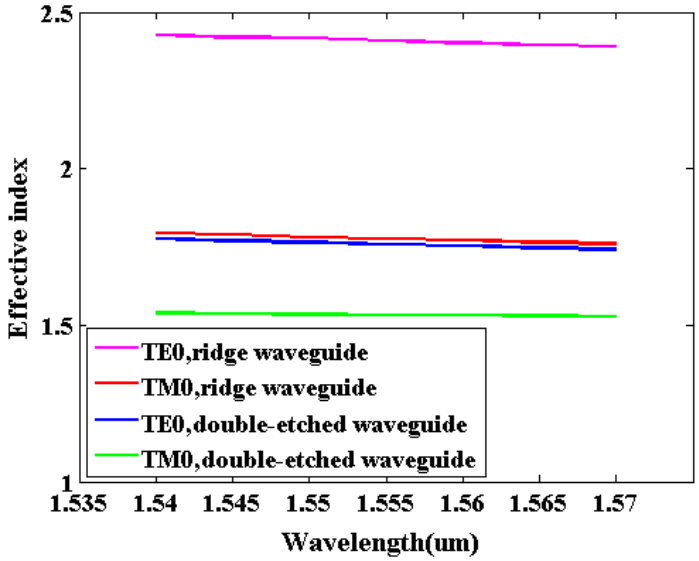

Figure 2.2. Effective indices at the coupling section vs. wavelength.

As can be seen from Figure 2.2, the effective indices of this directional coupler system met the two requirements that we discussed above. First, the effective index of the TM_0 mode in the ridge waveguide is very close to the effective index of the TE_0 mode in the double-etched waveguide. This ensures that there will be a very strong cross-polarization coupling for the TM_0 mode. Second, the effective index of the TE_0 mode in the ridge waveguide differs from the effective index of

the TE_0 mode in the double-etched waveguide so as to avoid coupling between these two modes.

To verify the behavior of this device, we performed three dimensional finite difference time domain (3D FDTD) simulation using Lumerical's FDTD solutions. As we can see from Figure 2.3(a), when launching TE_0 at the input port, the light will propagate along the ridge waveguide and comes out from the through port completely. On the contrary, as can be seen from Figure 2.3(b), when launching TM_0 mode from the input port, the light will couple to the double-etched waveguide and comes out from the cross port as TE_0 mode.

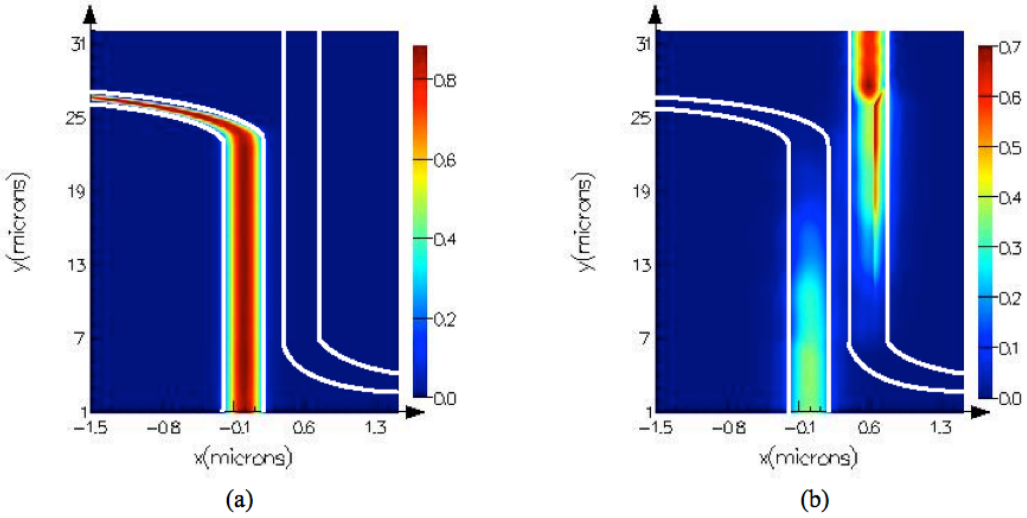

Figure 2.3. Simulation results for the intensity of light when launching (a) TE mode and (b) TM mode as the input.

To further illustrate the TM_0-to-TE_0 mode coupling-and-conversion process, we have shown the total electric field distribution at different cross sections in Figure 2.4 (The locations of the four cross sections are shown in Figure 2.1, accordingly). As we can see from cross section (I), the mode power is mostly carried by the TM_0 mode in the left ridge waveguide, before entering into the coupling section. But it is also obvious that some optical power has started to transfer to the double-etched waveguide in the right-hand side. At section (II),

which is at the end of the coupling section, most optical power has been coupled to the double-etched waveguide in the right-hand side. At section (III), due to the bend at the output section, the two waveguides are separated further, and the optical power is mostly carried by the double-etched waveguide. At section (IV), where there is no more ridge waveguide in the left, the double-etched waveguide has adiabatically converted into a ridge waveguide. As we can see very clearly, now the output power at the cross port is purely TE_0 mode.

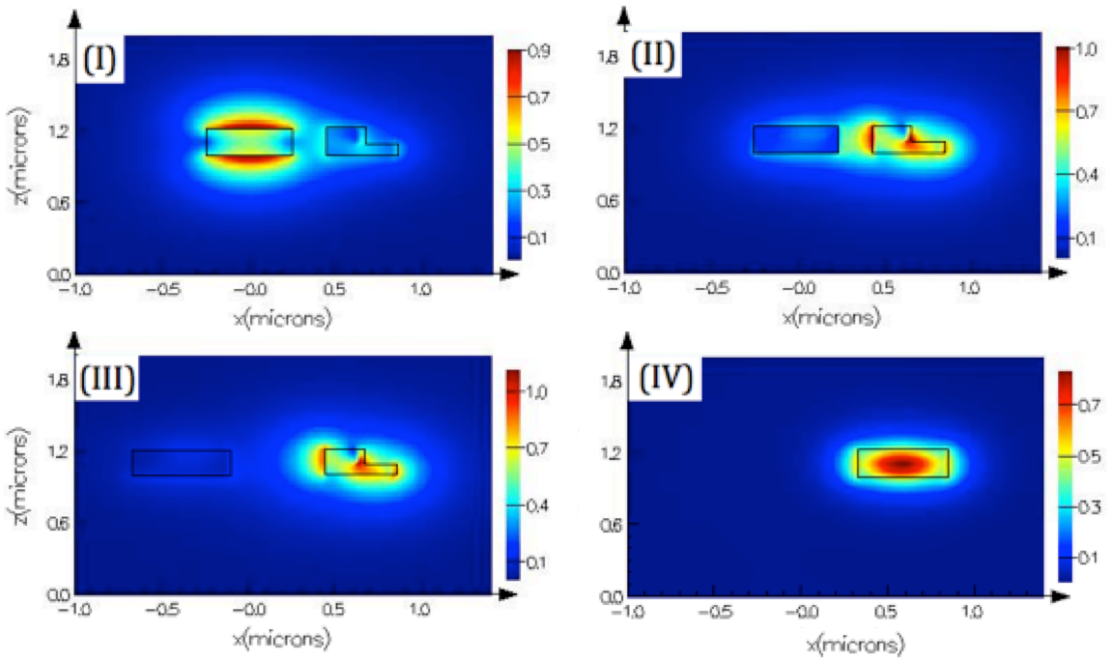

Figure 2.4. Total electric field amplitude (|E|) profile as the input TM0 field travels through the PSR

2.3 Fabrication of the polarization splitter-rotator with the calibration structures.

This device is fabricated on an 8-inch SOI wafer using Optoelectronic Systems In Silicon (OpSIS) Multi-Project Wafer (MPW) Shuttle runs.

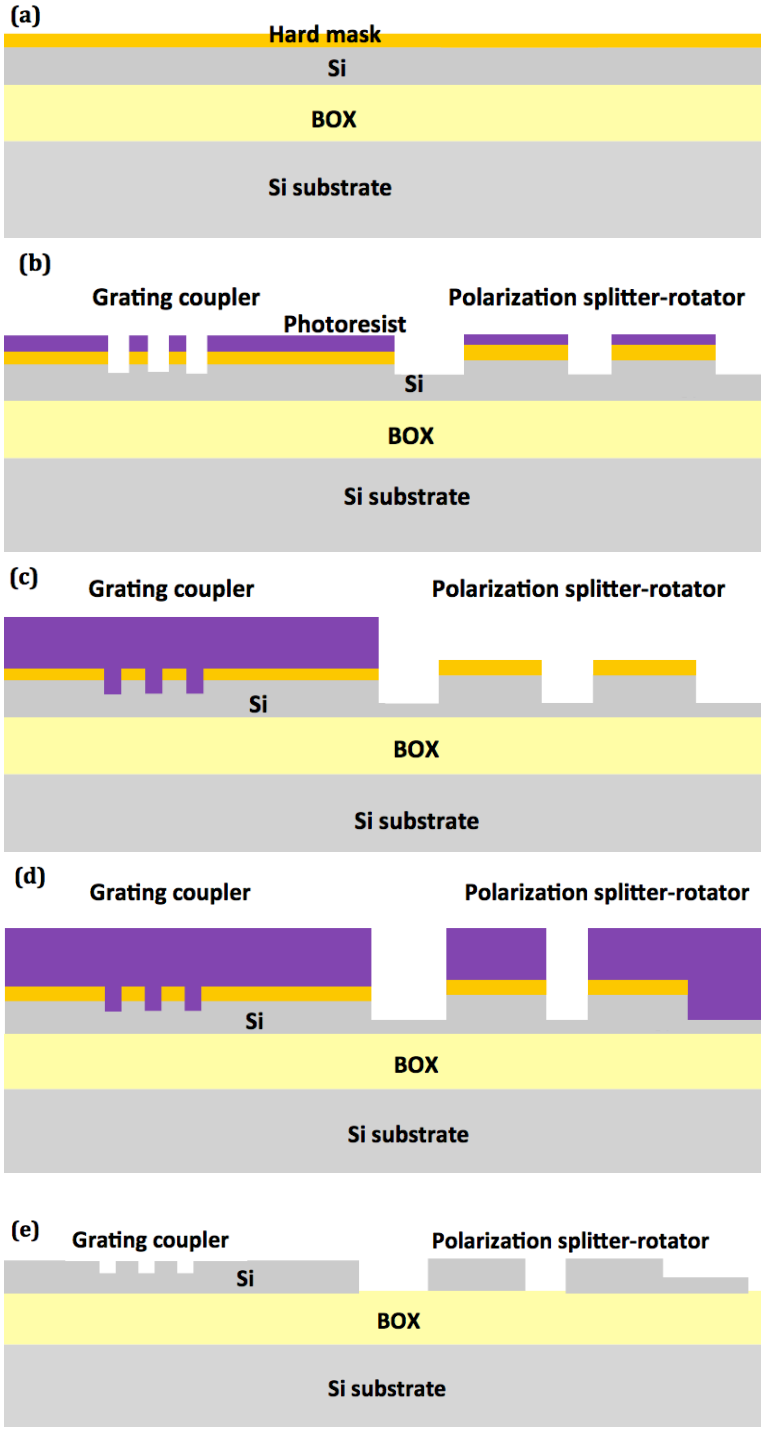

Figure 2.5. Process flow (a) starting on a 220 nm SOI wafer, PECVD hard mask (b) lithography step 1, etch depth = 60 nm (c) lithography step 2, etch depth = 70 nm (d) lithography step 3, etch depth = 90 nm (e) strip photoresist and hard mask

The wafer is a 220 nm thick silicon film on top of a 2 μm thick buried oxide layer (BOX). The fabrication process flow is shown in Figure 2.5. Three masks were used to pattern the polarization splitter-rotator and also the grating couplers, which are used to test the devices. The first mark defined the 220 nm height silicon. And the second mask defined the 160 nm thick partially-etched silicon layer, which is used for the grating teeth. And the third mask is used to define the 90 nm thick partially-etched silicon layer. Finally, the un-patterned areas were fully etched to the BOX. And a silicon oxide layer is then deposited on top of the silicon devices, which is not shown in Figure 2.5.

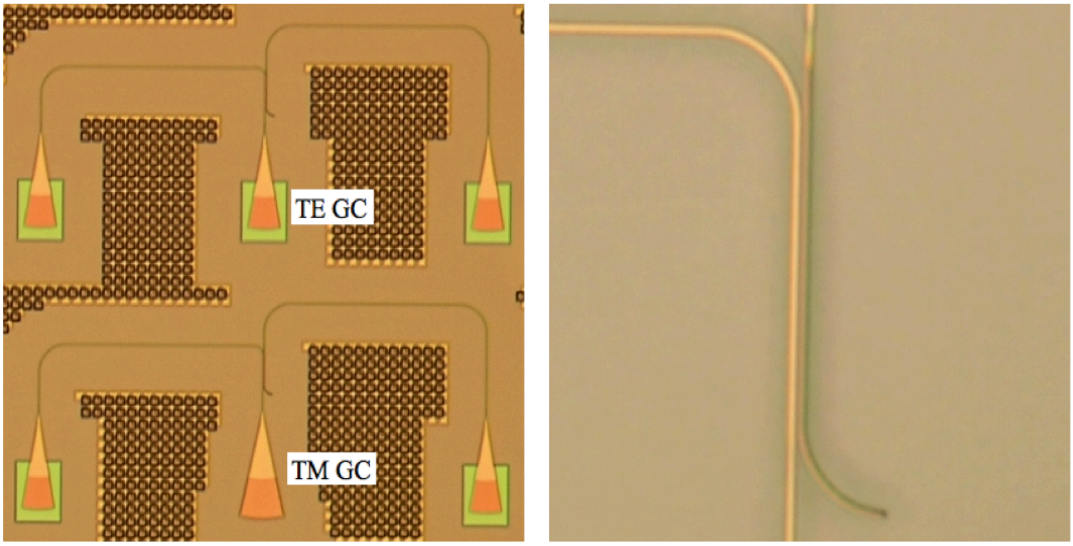

Figure 2.6. Optical micrograph of the fabricated devices (a) polarization splitter-rotator with two calibration structures (b) magnified polarization splitter-rotator

Figure 2.6(a) shows the fabricated polarization splitter-rotator with TE and TM grating couplers. The two calibrations structures are used to extract the loss and crosstalk. Both structures have three ports and use the center port as the input. The lower structure measures the response when inputting TM. Similarly, the upper structure measures the response when inputting TE. It should be noted

that while the types of grating couplers used in these two calibration structures are different, the polarization splitter-rotators are designed to be identical. Figure 2.6(b) shows a zoom-in picture of the polarization splitter-rotator. Although Figure 2.6(b) is blurry, we can still tell the ridge waveguide (yellow) from the double-etched waveguide (green) from this optical picture.

2.4 Measurement and results

This polarization splitter-rotator is characterized on a wafer scale test setup. The light is first generated from a tunable laser centered at 1550 nm and then goes through a polarization controller. After that, the light was coupled into the grating couplers, which are highly polarization dependent [60].

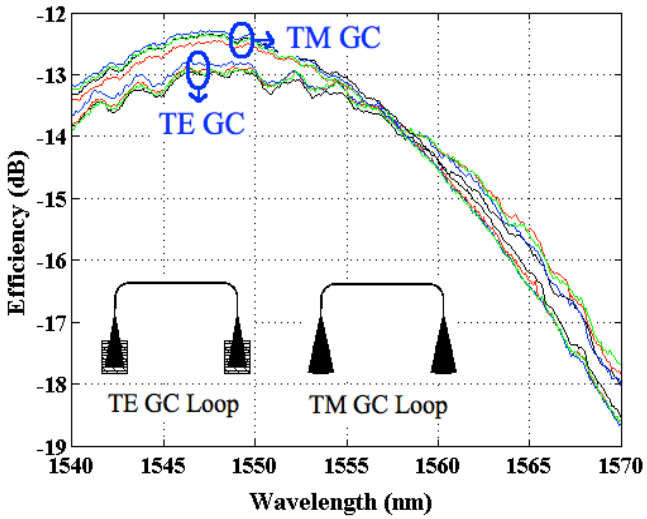

Figure 2.7. Spectral response of the TE and TM grating coupler loops.

The periodicities of the TE grating coupler and TM grating coupler is 0.63 μm with a 65% duty cycle and 0.93 μm with a 76% duty cycle, respectively. As shown in Figure 2.7, the peak coupling efficiency of the grating couplers are located at

1547 nm. More importantly, the spectral responses of both grating couplers are close to each other, with a maximum deviation of 0.3 dB.

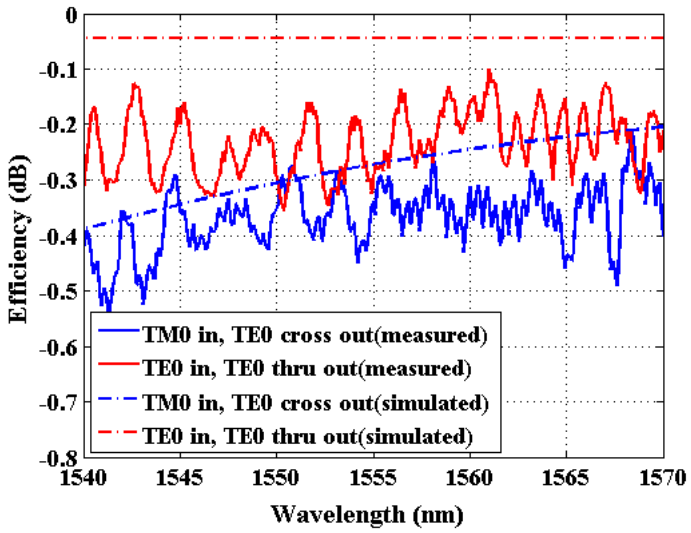

(a)

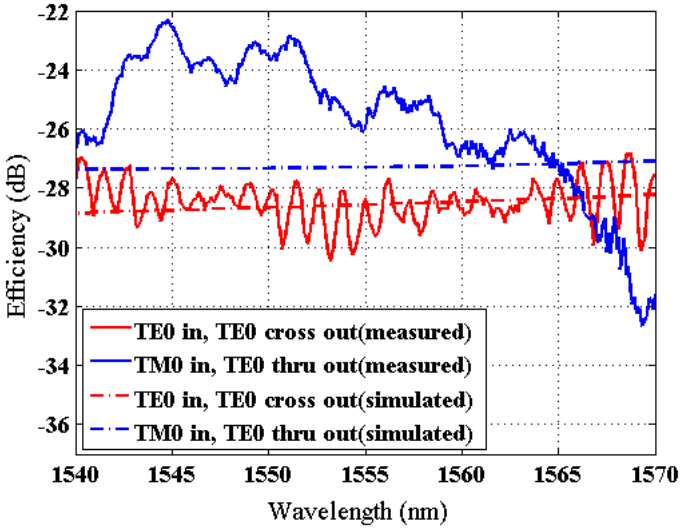

(b)

Figure 2.8. Measured and simulated spectra of the PSR with input and output grating loss normalized showing (a) conversion loss and (b) crosstalk.

To get the TM-to-TE polarization conversion loss and also the TE insertion loss, we need to subtract the losses caused by the grating couplers. Figure 2.8(a)

shows the simulated and measured TM-to-TE polarization conversion loss and also the TE insertion loss. It can be seen that the polarization splitter-rotator shows a measured polarization conversion loss better than 0.5 dB and a TE insertion loss better than 0.3 dB in the wavelength regime 1540 – 1570 nm. Figure 2.8(b) shows the polarization crosstalk at two output ports. For both polarization states, the crosstalk is below – 20 dB, which meets the requirements for most applications. In addition, we can see that the simulated results and the measured results match well.

2.5 Fabrication tolerance analysis

To investigate the fabrication tolerance of this device, we have selected five key geometry parameters and varied them within +/- 10 nm. As can be seen in Figure 2.9, the proposed polarization splitter-rotator exhibits a very good fabrication tolerance to W_1, W_3, and W_g. The polarization conversion efficiency does not experience any obvious changes with respect to the change of these parameters. However, it worth noting that this device is sensitive to the deviation of W_2 and H_2, even though the excess losses remain relatively modest for a deviation of W_2 as large as 10 nm. The main reason is that both W_2 and H_2 are key parameters to control the effective index of the TE_0 mode in the double-etched waveguide. In order to maintain high polarization conversion efficiency, we have to make sure that the effective index of the TE_0 mode in the double-etched waveguide are close to that of the TM_0 mode in the ridge waveguide. Thus, W_2 and H_2 are two extremely important parameters for the success of this device. Overall, this device is sensitive to fabrication tolerance, and may encounter problems for

massive production. However, the problem could be mitigated if we can make a precise control of the fabrication variations.

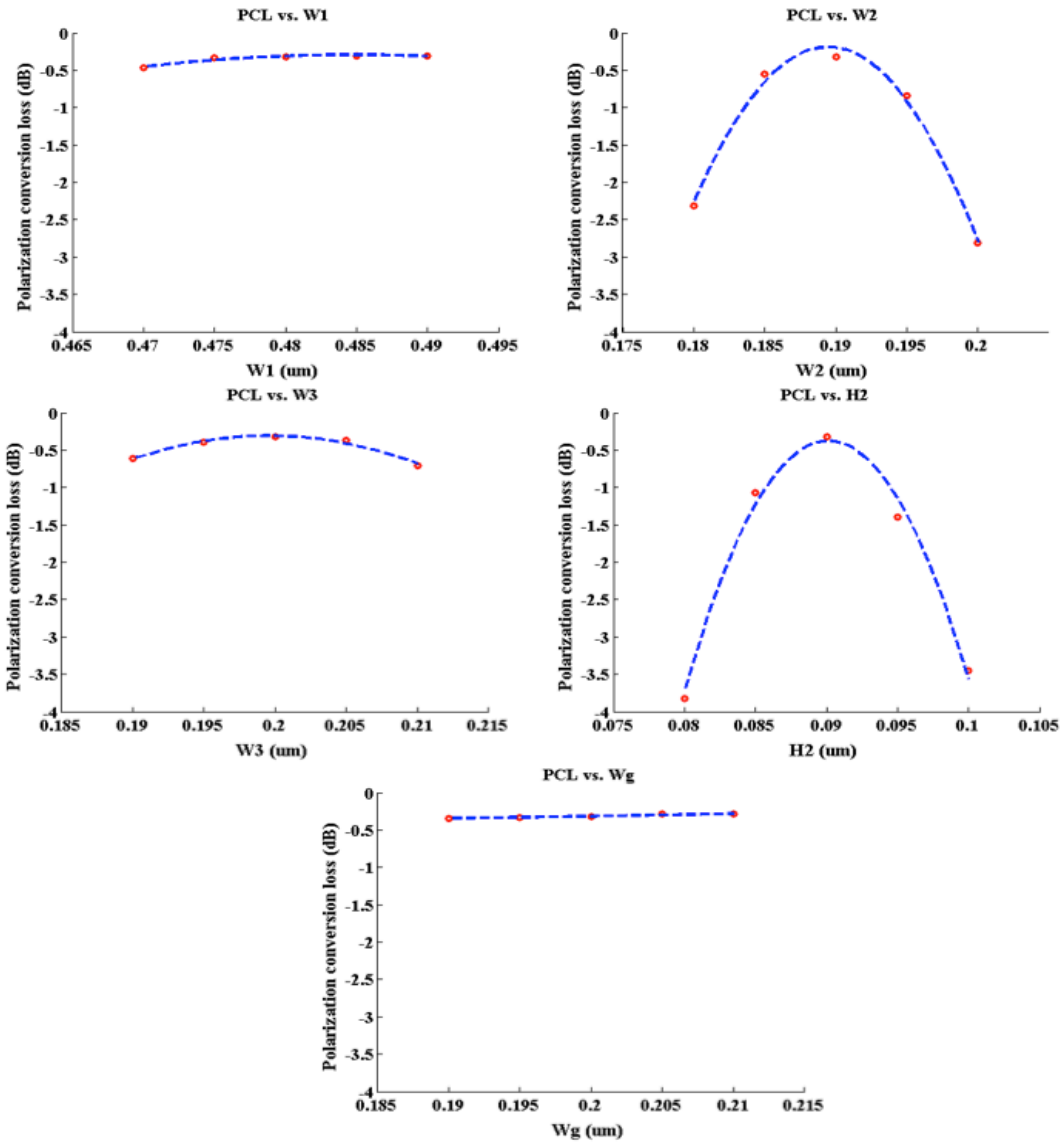

Figure 2.9. Polarization conversion loss vs. geometry parameter variation. (the red dots represent the simulated polarization conversion losses, and the blue curves represent the fits from these dots)

CHAPTER 3
POLARIZATION SPLITTER-ROTATOR WITH A MACH-ZEHNDER-BASED MODE CONVERTER

In chapter two, we have discussed a polarization splitter-rotator, which is based on a double-etched directional coupler. This polarization splitter-rotator has three characteristics: first, this device is based on the mode principle; second, the polarization separation process and polarization rotation process happen at the same time; third, this device is designed to work at C band (1530-1565 nm in optical communication). The C-band is the dominant band for long-haul optical networks. However, for short-distance optical communication, the O band (1260-1360 nm) becomes more and more important, especially for the communication in data centers. Thus, there is a need to design a high performance polarization splitter-rotator at O band, which could be used to implement polarization diversity circuits as we discussed earlier.

In this chapter, we will discuss a polarization splitter-rotator built on a 220 nm silicon-on-insulator platform using a 248 nm deep ultraviolet lithography. The polarization splitter-rotator also has three characteristics: first, this device is based on the mode evolution principle; second, the polarization separation process and the polarization rotation process happen separately, one after another; third, this device is designed for 1310 nm data communication (O band). Conceptually, there is no significant difference between the design of an O band and a C band polarization splitter-rotator. However, in terms of fabrication, there is some difference, because polarization splitter-rotator that works at O band has a smaller feature size than that at C band. Suppose we use the same lithography process to pattern these two polarization splitter-rotators, the device designed

for the O band would suffer a larger fabrication deviation as compared to the device designed for the C band.

3.1 Different polarization split and rotation principles

Actually, a polarization splitter-rotator could be recognized as a combination of two different devices – a polarization beam splitter (PBS) and a polarization rotator (PR). Suppose we cascade a high performance polarization beam splitter with a high performance polarization rotator, we should be able to get an excellent polarization splitter-rotator. In this section, we will give a brief introduction of PBSs and PRs. This will lay the foundation to create a novel polarization splitter-rotator in the next section.

Polarization beam splitters are used to separate the transverse electric (TE) and transverse magnetic (TM) polarizations. A detailed review of this device can be found in the literature [61]. To date, several kinds of waveguide type polarization beam splitters have been reported utilizing different structures, for example, Mach-Zehnder interferometers [62-65], multimode interferences [66-67], directional couplers [68-70] and photonic crystal [71-72]. In our design, we choose a directional coupler structure as a polarization beam splitter, because of its simplicity and compact footprint.

Polarization rotators are used to rotate one polarization state into the orthogonal polarization state. Generally, there are three categories of on-chip polarization rotators [73]. The first category is based on the mode coupling and conversion principles. Some representative works are usually composed of a double-etched waveguide with a cut corner [74-75]. The abrupt change of cross-sections shape will cause scattering and mode conversion. The second category is

based on mode evolution principles. Typically, a waveguide with an adiabatic geometry change is introduced. In the middle of this waveguide, there will be strong mode hybridization and conversion [76-78]. The last category is to use external materials to assist the rotation of the light sitting in the silicon nanowire [79-81]. Materials like silicon nitride, metal and etc. are commonly seen in this category of polarization rotators. It worth noting that air is also widely used as a top cladding to achieve polarization rotation. However, air is not preferred, since it makes the polarization rotator not compatible with any back-end-of-line processes and thus difficult to be integrated with other silicon photonic devices. In our design, which will be illustrated in the next section, we use a bi-level taper-based mode converter, which is based on the mode evolution principle.

3.2 Design of polarization splitter-rotator with a Mach-Zehnder-based mode converter

The polarization splitter-rotator is constructed with a directional coupler based polarization beam splitter [82, 83] and a polarization rotator, which is comprised of a bi-level taper-based mode converter [84] and a Mach-Zehnder based mode converter [85]. This is the first time that the aforementioned three building blocks have been put together to form a polarization splitter-rotator.

Figure 3.1 shows the schematic of the proposed polarization splitter-rotator. When launching TE_0 mode at the input port, the light will propagate the input waveguide and come out to the through port directly. When launching TM_0 mode at the input, the light will first be coupled to other side of the directional coupler. At this time, the coupled mode is still TM_0. After that, the TM_0 mode will go

though the bi-level taper and becomes TE_1 mode. Then, the TE_1 mode will be converted into TE_0 at the cross port by the Mach-Zehnder mode converter.

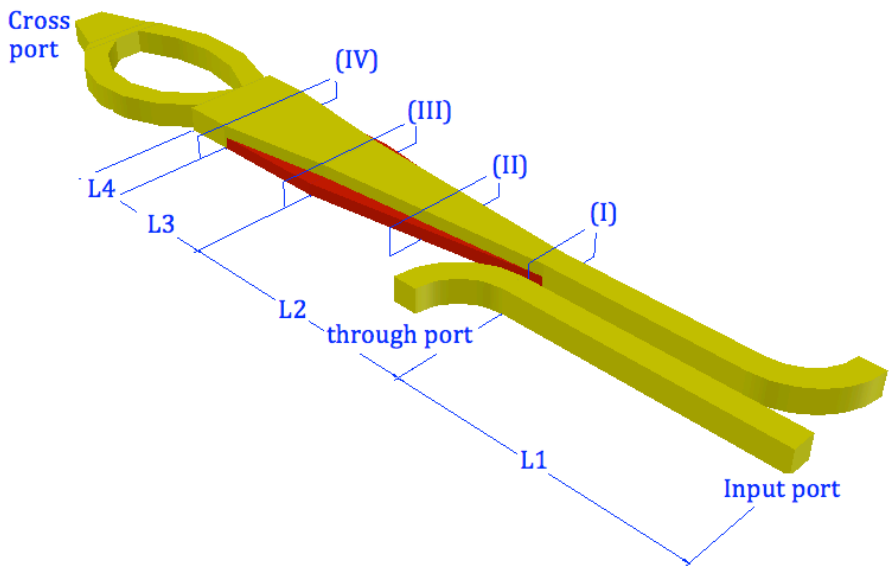

Figure 3.1. Schematic of the proposed polarization splitter-rotator

After optimization, we then fixed the values of the parameters that are shown in Figure 3.1. The thickness of the un-etched silicon is set to be H_1=220 nm (colored in yellow). And the thickness of the partially-etched silicon is set to be H_2=90 nm (colored in red). The symmetrical directional coupler is composed of two silicon nanowires (width W_1=400 nm, length L_1=15 nm, gap W_2=220 nm). The bend radius at the beginning of the right-side waveguide is 5 um, so the actual coupling length is L_C=10 μm. The bi-level taper consists of two sections. In the first section (L_2=19 μm), the un-etched waveguide width converts from W_1= 400 nm to W_2=620 nm. And the partially-etched waveguide width converts from W_1= 400 nm to W_3= 1.22 μm. In the second section (L_3=4 μm), the un-etched waveguide width changes to W_3=1.22 μm.

To verify the behavior of this device, we have launched 3D FDTD simulations using Lumerical FDTD solutions. Figure 3.2 shows the refractive indices of the

modes in the bi-level taper. As we can see, at the input of the bi-level taper (I), the refractive indices of the TM_0 mode and TE_1 mode are separated far away, so that mode hybridization will not happen at this time. But as the light propagates along the bi-level taper, the two refractive indices are becoming closer and closer. Between section (II) and (III), strong mode hybridization and conversion will happen. Now, the TM_0 mode will gradually change to TE_1 mode. When light comes to Section (IV), light will remain in the TE_1 mode and cannot be converted back to TM_0 mode, since the refractive indices are separated too far away.

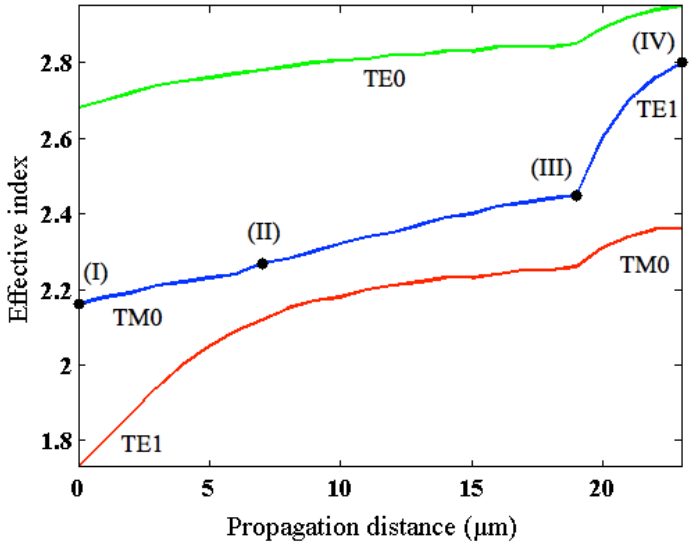

Figure 3.2. Mode index evolution along the bi-level taper.

To illustrate the mode conversion process in the bi-level taper, we have pictured the electric field distribution at the above four sections, as shown in Figure 3.3. As we can tell from plots (I) and (II), the mode is mainly TM_0. But when we take a look at plots (III) and (IV), it can be clearly observed that the mode is mainly TE_1. Figure 3.4 shows that this bi-level taper has a polarization conversion efficiency over 92% in the wavelength region 1290-1330 nm. The Mach-Zehnder has a TE1-to-TE0 mode-conversion efficiency of 82% at 1310 nm,

and the mode-conversion efficiency is larger than 78% in the aforementioned wavelength region.

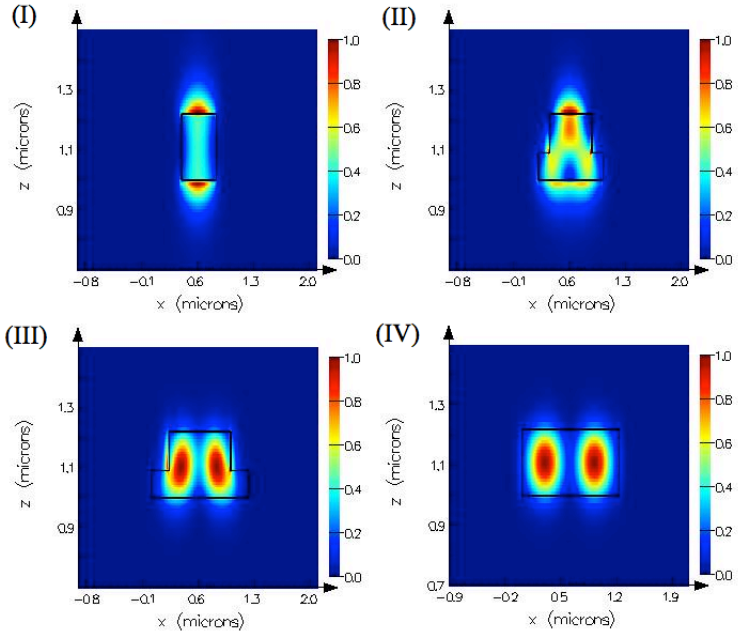

Figure 3.3. Total electric-field amplitude (|E|) changes as the input TM0 field travels through the bi-level taper. The above four subplots show the mode profiles at corresponding sections in Figure 3.1.

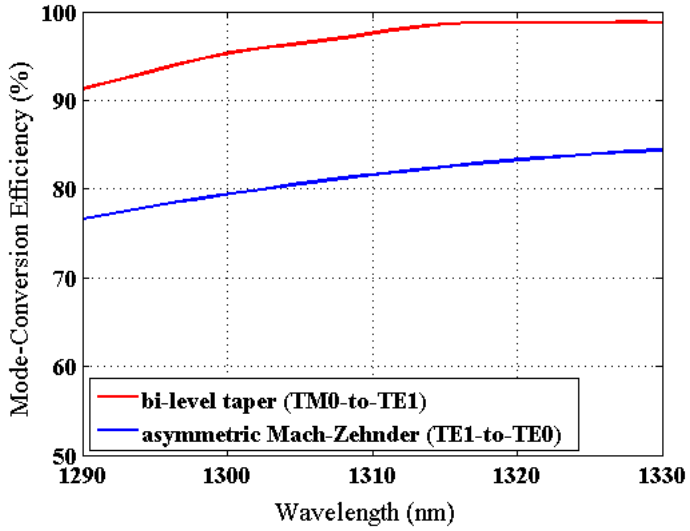

Figure 3.4 Simulated mode-conversion efficiencies of the bi-level taper and asymmetric Mach-Zehnder

3.3 Fabrication of the polarization splitter-rotator with the calibration structures

The fabrication details have been discussed in section 2.3. Here, we just show the pictures of the fabricated device in Figure 3.5.

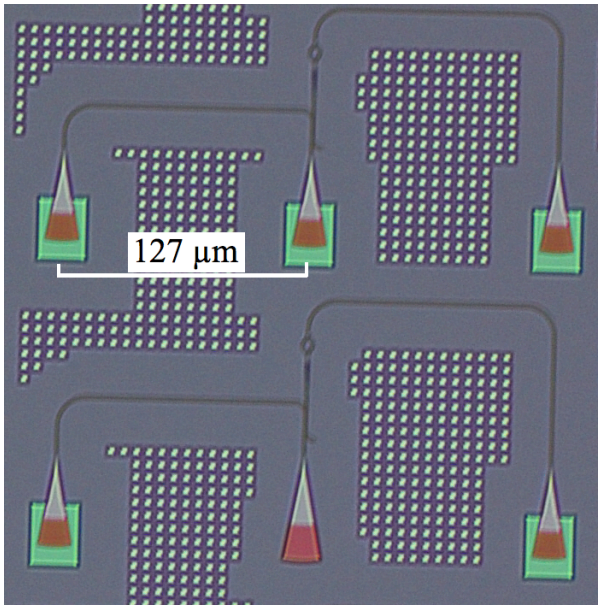

(a)

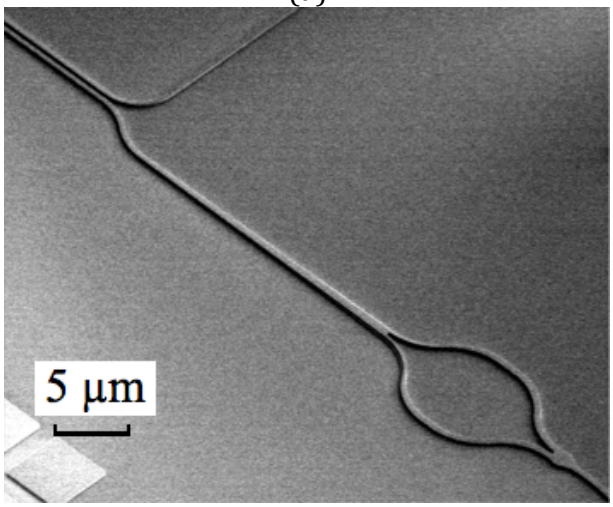

(b)

Figure 3.5. (a) Optical micrograph of two fabricated calibration structures, with PSRs designed to be identical. (b) Scanning electron microscope picture of the fabricated PSR.

3.4 Measurement and results

The measurement setup has been discussed in section 2.4. Figure 3.6 shows the spectral responses of the TE and TM grating coupler loops. The TM grating coupler has an average coupling loss of 7.6±0.05 dB at 1310 nm, while the TE grating coupler has an average coupling loss of 8.9±0.05 dB at 1310 nm.

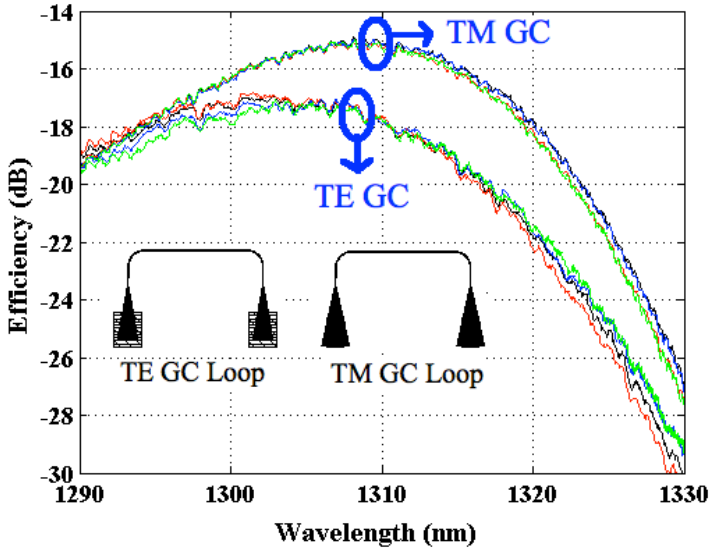

Figure 3.6. Spectral responses of the TE and TM grating coupler loops. The spectra of the four loops were averaged and then used to extract the PSR losses.

As shown in Figure 3.7(a), the polarization splitter-rotator shows a better than 2 dB polarization conversion loss and a 0.5 dB TE insertion loss. We measured the crosstalk to be better than 20 dB as shown in Figure 3.7(b).

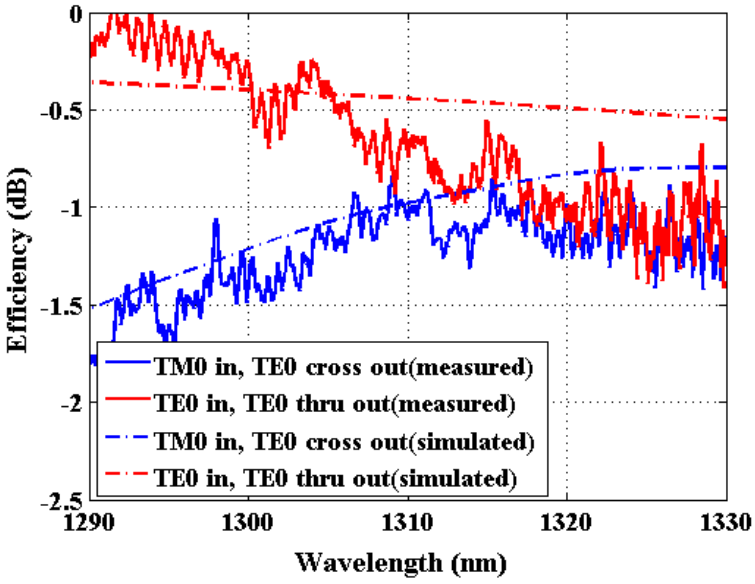

(a)

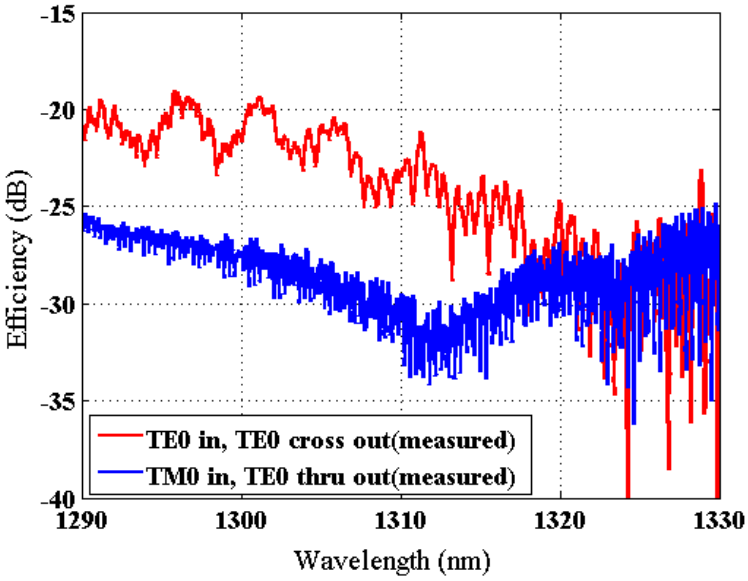

(b)

Figure 3.7. Measured and simulated spectra of the PSR with input and output grating losses normalized, showing (a) conversion loss and (b) crosstalk.

CHAPTER 4
BI-WAVELENGTH POLARIZATION SPLITTER-ROTATOR

In the previous two chapters, we have demonstrated two polarization splitter-rotators. One of them works at 1550 nm wavelength region, and the other works at 1310 nm wavelength region. To date, most polarization splitter-rotators work in silicon [81,93-95] has been focused on the 1550 nm wavelength region. However, in some applications, we need a polarization splitter-rotator to work at two widely separated wavelength regions (e.g. at both 1310 nm and 1550 nm). Then, the question is how to design a high-efficiency bi-wavelength polarization splitter-rotator that caters to such a stringent requirement. This is a challenging topic, which has not been sufficiently addressed in the literature.

In this chapter, we describe the first theoretical demonstration of a bi-wavelength PSR, which is designed to work in both the 1310 nm and 1550 nm wavelength ranges. The PSR is composed of a wideband bi-level TM_0-to-TE_1 mode converter and an asymmetric directional coupler. Similar geometries have been proposed in the literature [46, 84], and experimentally demonstrated in the literature [41, 78, 94, 95] for single wavelength operation. Here, we engineered this geometry to work at two distinct wavelengths bands for the first time. We believe that combining this PSR with a low-loss and wideband edge coupler can offer a high-efficiency edge-coupling-based light duplexing solution.

4.1 Introduction of bi-wavelength coupling

Wavelength-division-multiplexed passive optical networks (WDM PONs) are regarded as a potential solution for next generation optical access networks due

to their high bandwidths [86]. However, the relatively high cost of WDM PON is still one of the main limitations of its practical usage. Recently, many researchers have shifted their attention to silicon-on-insulator (SOI) based integrated circuits that could offer a high-density integration with a relatively low cost for mass production [43-44].

Today's fiber-to-the-home (FTTH) systems usually utilize two different wavelengths for upstream and downstream traffic. Typical operation wavelengths are near 1310, 1490, or 1550 nm, which are widely spaced. Thus, one important issue of implementing WDM PON system on a SOI platform is to find an efficient mechanism to duplex light. To this end, both 1-D and 2-D bi-wavelength grating couplers [87-90] have been proposed. 1-D bi-wavelength grating coupler for 1310 and 1490 nm wavelengths with a -2.5 dB insertion loss has been demonstrated in [87]. Xu et al. demonstrated a 2-D bi-wavelength grating coupler with -6 dB and -6.5 dB insertion losses for 1490 and 1550 nm [88]. To further solve the polarization dependent loss problem of bi-wavelength grating coupler, Streshinsky et al. recently experimentally demonstrated the first bi-wavelength polarization-splitting grating coupler with a insertion loss of -8.2 dB and -7.1dB at 1310 nm and 1550 nm, respectively [90]. Although grating-coupling-based light duplexing mechanisms have been widely discussed, the insertion loss of this mechanism is still relatively high.

Instead of using a grating-coupling-based light duplexing mechanism, it is also possible to develop an edge-coupling-based light duplexing mechanism. However, there has been no demonstration of a light duplexing mechanism where light is coupled into the chip through an edge coupler thus far. To achieve such an edge-coupling-based light duplexing mechanism, both a wideband edge coupler and a bi-wavelength polarization splitter and rotator (PSR) are needed.

Low-loss and wideband edge couplers have been demonstrated in the literature [91-92]. Also, PSRs centered at 1550 nm with a wide bandwidth (e.g. 60 nm ~ 80 nm) have been demonstrated in the literature [81,93-95]. However, to our best knowledge, bi-wavelength PSRs which can work at two widely separated wavelengths have not been demonstrated thus far.

4.2 Bi-wavelength polarization splitter-rotator

The schematic of the bi-wavelength PSR is shown in Figure 4.1, where the yellow regions represent the un-etched Si waveguide and the blue regions represent the partially etched slab waveguide. The un-etched Si thickness is H_1=220 nm, while H_2 to represent the thickness of the partially etched slab waveguide.

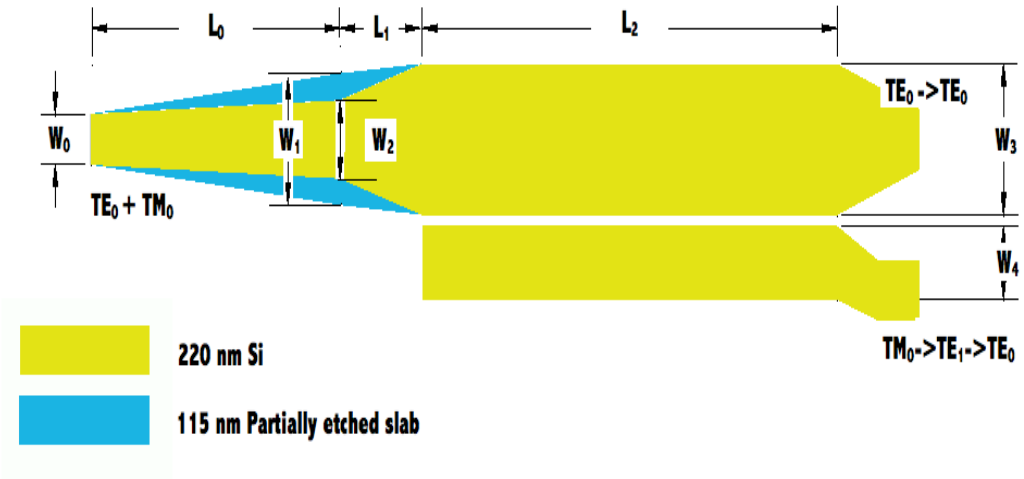

Figure 4.1. Schematic of the proposed bi-wavelength PSR with significant geometric parameters noted.

This device is composed of a wideband TM_1-to-TE_1 mode converter, an asymmetric bi-wavelength directional coupler and a symmetric SiO_2 cladding. Detailed description of the working principle of this device can be found in the

literature [46, 95]. Both the TE_0 and TM_0 modes are launched into the left port of the bus waveguide, as shown in Figure 4.1. The TE_0 mode will pass through the bus waveguide and comes out from the right port of the bus waveguide directly. Meanwhile, the TM_0 mode will be converted to the TE_1 mode after passing through the bi-level taper, and then be coupled into the access waveguide to become the TE_0 mode when passing through the asymmetric directional coupler.

However, there are two major problems that need to be solved in order for this geometry to work at two widely separated wavelengths. The first problem is how to make a bi-level TM_0-to-TE_1 converter not only highly efficient, but more importantly, ultra-wideband. The fundamental principles of designing a highly efficient bi-level TM_0-to-TE_1 converter have been discussed in the literature [84], but, how to design a wideband converter, which can cover two widely separated bandwidths, has never been discussed before. In section 4.2.1, we use the particle swarm optimization (PSO) method to design an ultra-wideband mode converter, which has a minimum TM_0-to-TE_1 mode conversion efficiency of 96% in the wavelength region of 1250 – 1600 nm (350 nm bandwidth). The second problem is how to design a bi-wavelength asymmetric directional coupler. To be more specific, the difficulty is to size the widths of the directional coupler so that the phase-matching conditions are satisfied at two widely separated bandwidths.

4.3 Design of wideband bi-level taper

The PSO method has been widely used in today's optical device designs to find the optimum geometries [11-12]. To design a wideband bi-level taper, the geometry parameters (W_0, W_1, W_2, L_0, L_1, and H_2) need to be optimized. The other two parameters are fixed (H_1=220 nm and W_3=1.25 μm). The optimization figure

of merit (FOM) for the bi-level taper is defined as normalized TE_1 mode power transmission at a certain wavelength, written as FOM_λ. In the optimization, we first chose 10 wavelength points across a 350 nm range (1250 - 1600 nm) and take the average of FOM_λ as FOM_{avg}. Then, we maximized FOM_{avg} to get the optimum geometry parameters for the wideband bi-level taper [19]. After optimization, we choose W_0=0.40 μm, W_1=1.085 μm, W_2=0.645 μm, L_0=40 μm, L_1=4 μm, and H_2=115 nm.

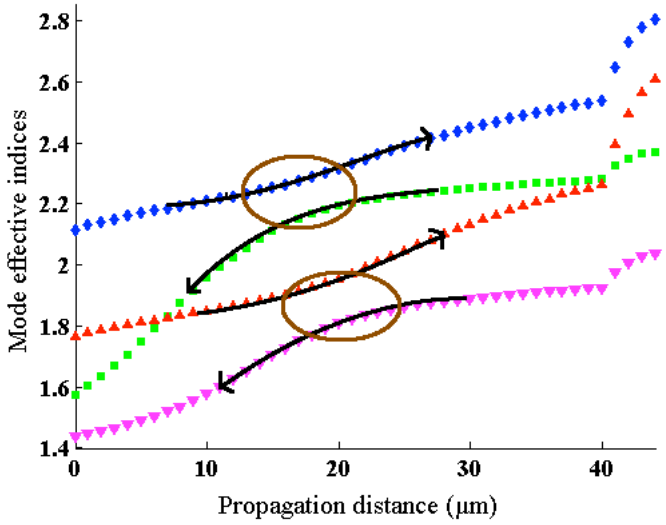

Figure 4.2. Mode index evolution along the PR structure.

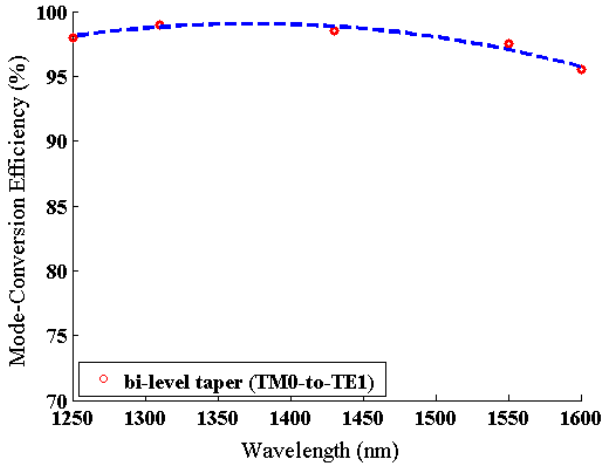

Figure 4.3. Simulated mode-conversion efficiencies of the bi-level taper

Figure 4.2 shows the effective indices of the TM_0 mode and the TE_1 mode at both wavelengths as light propagates through the bi-level taper. As shown in Figure 4.2, the effective index of the TE_1 mode curve is close to the TM_0 mode curve at around 20 μm, where strong mode hybridization and conversion occur. After traveling through this section, the input TM_0 mode converts to the TE_1 mode at both wavelengths. Figure 4.3 shows the simulated mode conversion efficiency in the wavelength regime 1250-1600 nm. As can be seen from Figure 4.3, the overall mode conversion efficiency is above 96% in the wavelength regime of 1250-1600 nm.

4.4 Design of bi-wavelength asymmetric directional coupler

The design of a bi-wavelength directional coupler comprises two steps. The first step is to choose a pair of waveguide widths so that the phase matching conditions are satisfied at both wavelengths.

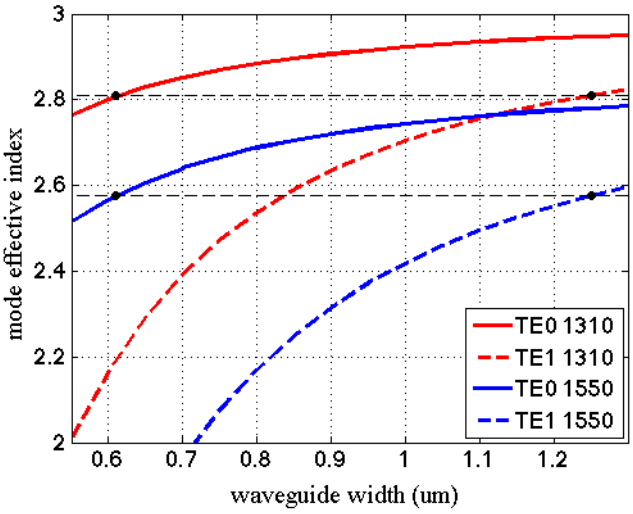

Figure 4.4. Effective indices at the coupling section vs. wavelength.

Figure 4.4 shows the effective indices of the TE_0 mode and TE_1 mode at both wavelengths as a function of waveguide width. When choosing the bus waveguide width W_3=1.25 μm and the access waveguide width W_4=0.61 μm, the effective indices of TE1 mode in the bus waveguide are n_{eff} = 2.577 at 1550 nm and n_{eff} = 2.810 at 1310 nm. Meanwhile, the effective indices of TE_0 mode in the access waveguide are n_{eff} = 2.577 at 1550 nm and n_{eff} = 2.808 at 1310 nm, as marked by the four black dots in Figure 4.4. So we can conclude that the phase-matching conditions for both wavelengths are simultaneously satisfied, which ensure that almost 100% power will be transferred to the other waveguide.

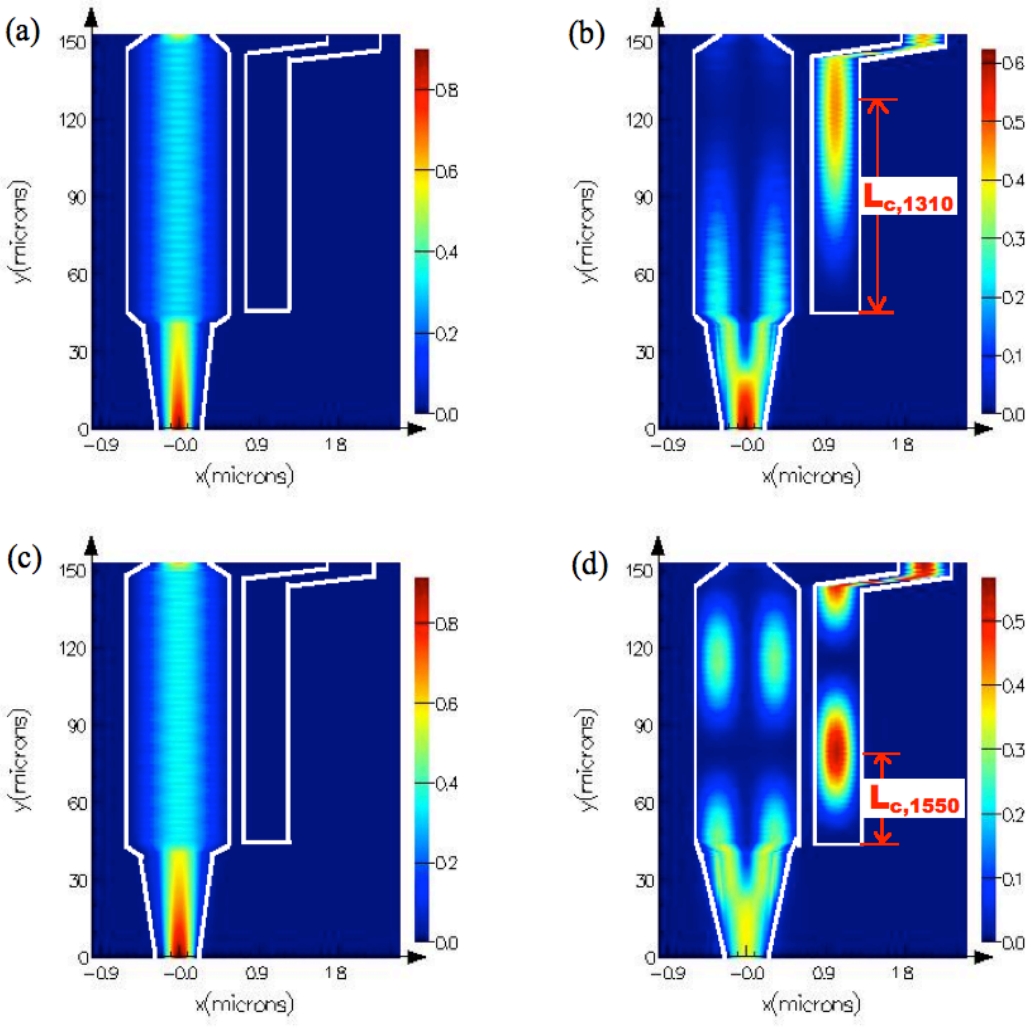

Figure 4.5. Mode propagation when launching (a) TE_0 at 1310 nm, (b) TM_0 at 1310, (c) TE_0 at 1550 nm, and (d) TM_0 at 1550 nm.

The second step is to engineer the gap (W_g) between the two waveguides so that at both wavelengths, the TE_1 mode in the bus waveguide could be coupled into the TE_0 and comes out from the access waveguide. By varying W_g, the coupling length for both wavelengths ($L_{C,1310}$ and $L_{C,1550}$) will change accordingly. To verify the behavior of this device, 3-D FDTD simulation was performed. Figure 4.5 shows the mode profile when launching TE_0 and TM_0 at both wavelengths. As can be seen from Figure 4.5(b) and Figure 4.5(d), the maximum power coupled into the access waveguide occurs at 130 μm in 1310 nm and at 145 μm in 1550 nm. To reach a compromise, we end this directional coupler at 138 μm (L_2=94 μm), so that both wavelengths have relatively high coupling efficiencies. Figure 4.6 shows the TM_0-to-TE_0 polarization conversion loss (PCL) near wavelengths 1310 nm and 1550 nm. As shown in Figure 4.6, the proposed PSR has a simulated minimum insertion loss of -0.9 dB near 1310 nm and -1.0 dB near 1550 nm. It is also worth noting that the PCL changes relatively less in the transmission window near 1310 nm than it does near 1550 nm.

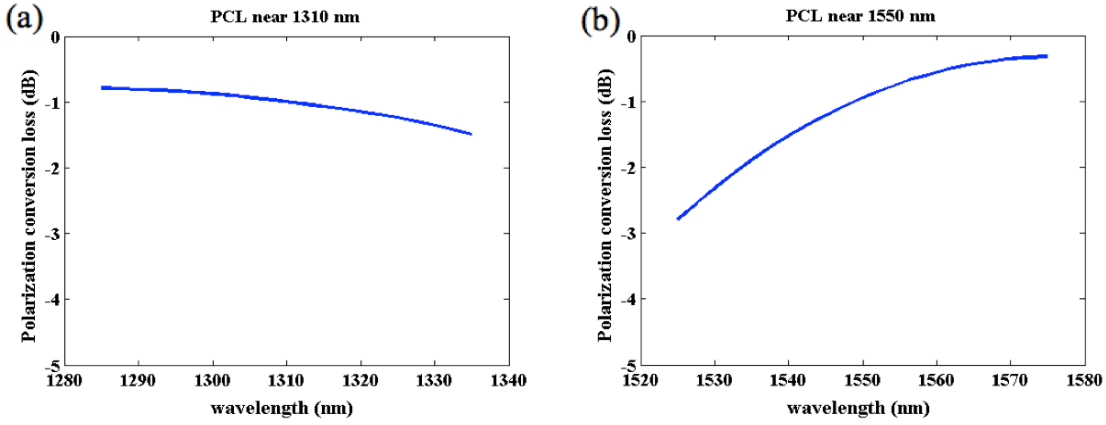

Figure 4.6. Simulated polarization conversion efficiency near wavelengths (a) 1310 nm and (b) 1550 nm.

4.5 Fabrication tolerance analysis

To investigate the fabrication tolerance, three key geometry parameters (W_3, W_4, and W_g) have been varied within +/- 5 nm. As shown in Figure 4.7, the polarization conversion loss (PCL) is less sensitive to W_3 and more sensitive to W_g and W_4. Also, as can be seen from Figure 5.7(b), the PCL at 1310 nm increases as W_g increases, while the PCL at 1550 nm decreases as W_g increases. The PCLs at both wavelengths reach a compromise at W_g=90 nm. The situation for W_4 is similar, as can be seen from Figure 4.7(c).

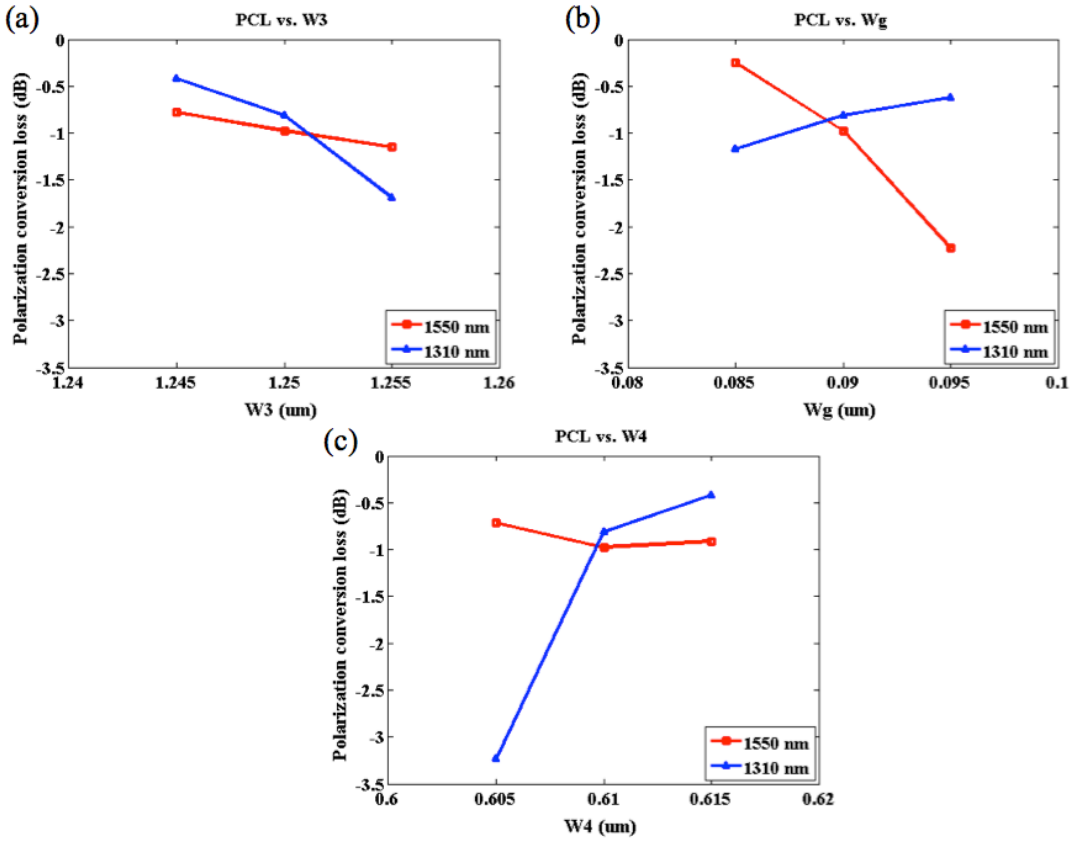

Figure 4.7. Polarization conversion loss vs. geometry parameter variation of (a) W_3 (b) W_g and (c) W_4

It worth noting that for each of these geometry parameters, there is a trade-off between the PCL at 1310 nm and the PCL at 1550 nm. Basically, the three key parameters that we choose are not the best for a single wavelength region, but they are the best if you take both wavelength regions into consideration. In addition, it is also evident that this device is relatively sensitive to fabrication deviations. Generally, optical lithography could introduce a more than 10 nm three-sigma deviation. This device experiences a severe PCL degradation within +/- 5 nm. So further optimization is needed to make this device more fabrication-insensitive.

CHAPTER 5
ULTRA-COMPACT POLARIZATION ROTATOR OPTIMIZED BY PARTICLE SWARM OPTIMIZATION

In the previous three chapters, we have discussed three different polarization splitter-rotators. In this chapter, we will discuss the design of a polarization rotator, which is another device for the implementation of polarization-diversity circuits. Actually, on-chip polarization rotators have been demonstrated using different materials, e.g. III-V materials [96-97], silicon/silicon dioxide [75, 77], photonics crystals [98], and plasmonic materials [99-101].

However, it is still difficult to achieve polarization rotators with both compact footprints and high polarization conversion efficiencies, while at the same time being CMOS-compatible. For example, Chen *at al.* [53] demonstrated a high efficiency polarization rotator on a hybrid Si/Si_3N_4-on-insulator platform, with a device length of 420 μm. Sacher *at al.* [25] demonstrated a high-efficiency polarization splitter-rotator based on an adiabatic bi-level taper and an asymmetric directional coupler with a device length of 475 μm. Both of the above demonstrations achieved very high efficiency based on the mode-evolution principles, but the footprints of these devices are still quite large. In addition, Chen *at al.* [102-103] proposed that it is possible to use an ultra-short slot waveguide to achieve a high polarization conversion efficiency. However, due to the lack of experimental results, we cannot conclude that this is a clear path to achieve our goal. Finally, surface plasmon polariton based polarization rotators [99-101] have received much attention recently. Although the footprints of these demonstrations are usually around ten microns, the insertion losses of these

devices are still high. Also, there are still some fabrication barriers that need to be overcome in order to make these devices fully compatible with CMOS process.

In this chapter, we will discuss an ultra-compact and high-efficiency polarization rotator built on a silicon-on-insulator platform. The polarization rotator is based on a bi-level taper TM_0-to-TE_1 mode converter and a bent-taper TE_1-to-TE_0 mode converter. The device is fully optimized by the particle swam optimization method and has a streamlined shape. This device could be easily fabricated using a CMOS-compatible process, and we believe that this device could be widely used in future's industrial applications.

5.1 Principle of the polarization rotator

The schematic of the proposed polarization rotator is shown in Figure 5.1. The proposed polarization rotator is comprised of an ultra-short bi-level taper and a bent taper. And a symmetric SiO_2 cladding surrounds the device.

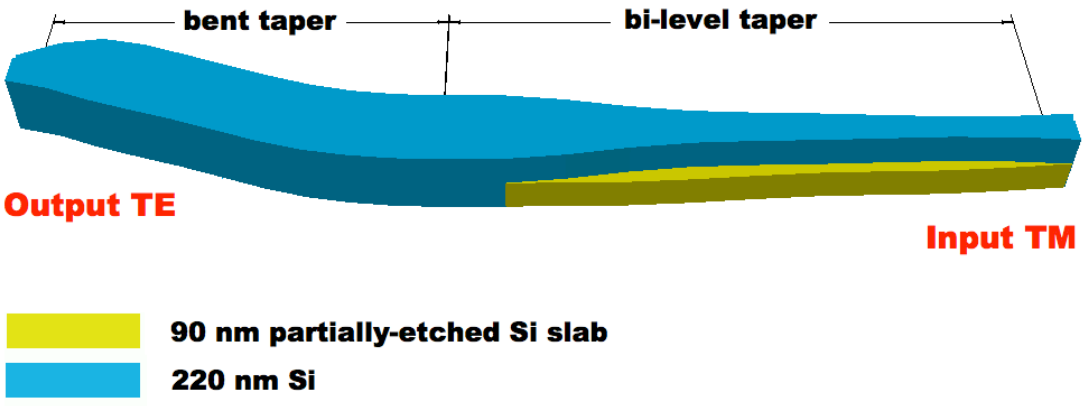

Figure 5.1. Schematic of the PR, consisting of a bi-level taper and a bent taper. The PR is surrounded by a symmetric SiO_2 cladding (a buried oxide bottom-cladding and a SiO_2 top-cladding).

This device is based on the widely used mode-evolution theory. However, there is a significant difference between this device and other mode-evolution based devices. Typical mode-evolution based devices [78, 104] sacrifice the footprints to achieve high mode conversion efficiency, such that the lengths of these devices are usually around hundreds of microns. In the next sections, we will demonstrate that it is possible to achieve a high mode conversion efficiency without compromising the footprints. In principle, the launched TM_0 mode will gradually change into the TE_1 mode when passing through the bi-level taper and then convert into the TE_0 mode with the assistance of the bent taper.

In order to achieve a compact footprint, we use particle swarm optimization to find the optimum geometric parameters. FDTD simulation could work in conjunction with evolutionary optimization algorithms to help find the optimum geometry parameters. Sanchis et al. demonstrated a high performance waveguide crossing using FDTD and genetic algorithm [105]. Particle swarm optimization is another commonly used evolutionary computing algorithm, which was first inspired by the social behavior of flocks of birds or schools of fishes [106], and has been applied to solve electromagnetic optimization problems [107]. Particle swarm optimization has been shown to be a very effective technology in designing compact and high-efficiency photonics devices, e.g. Y-junctions [11], crossings [12], and diffraction gratings [108-109]. Here, we use a built-in particle swarm optimization in Lumerical's FDTD solutions [110] to optimize the polarization rotator. The following sections are organized as follows: we first describe the optimization of the bi-level taper; then, we describe the optimization of the bent taper. Lastly, we combined these two components and simulated the performance of the polarization rotator using 3D FDTD simulation.

5.2 Design of a bi-level TM_0-to-TE_1 mode converter

The design of a linear bi-level TM_0-to-TE_1 mode converter has been discussed in literature [77, 84]. However, the lengths of such linear bi-level tapers are usually around a hundred microns or even longer.

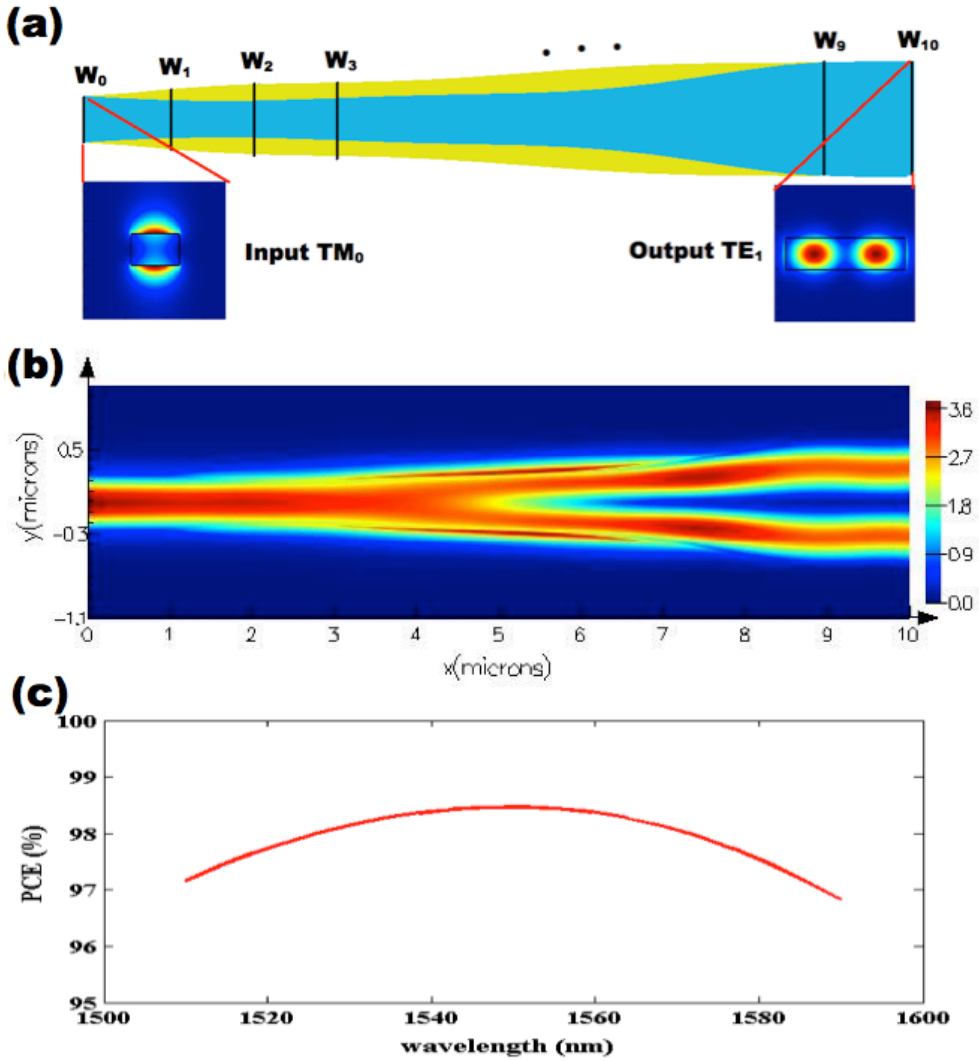

Figure 5.2. (a) Schematic of the bi-level taper (top view). The taper geometry is defined by spline interpolation of W_0 to W_{10}. (b) Simulated power distribution at 1550 nm wavelength. (c) Simulated PCE.

Here, we demonstrated for the first time that by utilizing a nonlinear bi-level taper, the length of the bi-level taper can be shrunk to ten microns, which is one order of magnitude smaller than the previous ones. As shown in Figure 5.2(a), the taper length is first set to be 9 μm. And the taper is then digitalized to 10 segments with interpolations between one and another, similar to the published techniques [11-12]. Since the bi-level taper has two layers: one is the 220 nm thick un-etched waveguide (colored in blue); the other is the 90 nm thick partially-etched waveguide (colored in yellow), we have 22 unknown parameters in total. The software updated the population (population size = 50) before the next run of simulations. After about 30 generations, the figure of merit (mode conversion efficiency) became stable. And the best individual has been selected out. Table I shows the values of the parameters after optimizations.

Table I. Taper width in nm

	W_0	W_1	W_2	W_3	W_4	W_5
Ridge	500	413	401	457	518	554
Slab	500	648	759	795	848	960

	W_6	W_7	W_8	W_9	W_{10}
Ridge	624	807	1077	1248	1250
Slab	1096	1191	1225	1237	1250

To verify the performance of the bi-level taper, we performed 3D FDTD simulations in Lumerical. The refractive indices of Si and SiO_2 at 1550 nm are 3.476 and 1.445, respectively. As shown in Figure 5.2(b), when we launch the TM_0 mode from the left-hand side, the TM_0 is efficiently converted into the TE_1 mode at the right-hand side. As shown in Figure 5.2(c), the polarization conversion efficiency (PCE) is higher than 97% over the bandwidth of 80 nm centered at 1550 nm. It worth noting that, if we change the length of the bi-level

taper to a larger value, e.g. 12 μm, and then perform the particle swarm optimization, the polarization conversion efficiency of the optimum geometry is expected to increase accordingly, because a longer length will contribute to a more sufficient conversion. The reason why we pick up the length of the bi-level taper to be 9 μm is because this is a good trade-off between the footprint and the performance.

5.3 Design of a TE_1-to-TE_0 mode converter

In this section, we will discuss the optimization of a TE_1-to-TE_0 mode converter. There are a variety of TE_1-to-TE_0 mode conversion schemes, e.g. directional couplers [111-112], multimode interferences [94], microrings [36], and asymmetric Mach-Zehnder interferometers [85]. However, most of above mode conversion schemes are sensitive to fabrications, especially for the Mach-Zehnder interferometers-based ones, since they depend on the exact phase-delay between arms. In addition, some of above mode conversion schemes are bandwidth-limited, especially for the microring-based ones.

Here, we demonstrate for the first time a wideband, fabrication-tolerant, compact and highly efficient TE_1-to-TE_0 mode converter based on a S-shaped ridge waveguide. The schematic of the proposed design is shown in Figure 5.3(a). The initial shape is a normal S-bend, which is defined by three parameters: center radius R_0, vertical offset dy, and waveguide width W. However, in order to perform particle swarm optimization, we digitalized the S-bend into 9 segments of equal angles, $d\theta$. The center radius R_0 divides the S-bend into two sides: the up side and the down side. Therefore, we have two sets of independent width

parameters: {W_{u1}, W_{u2}, W_{u3}, …, W_{u9}} and {W_{d1}, W_{d2}, W_{d3}, …, W_{d9}}, as indicated in Figure 5.3(a).

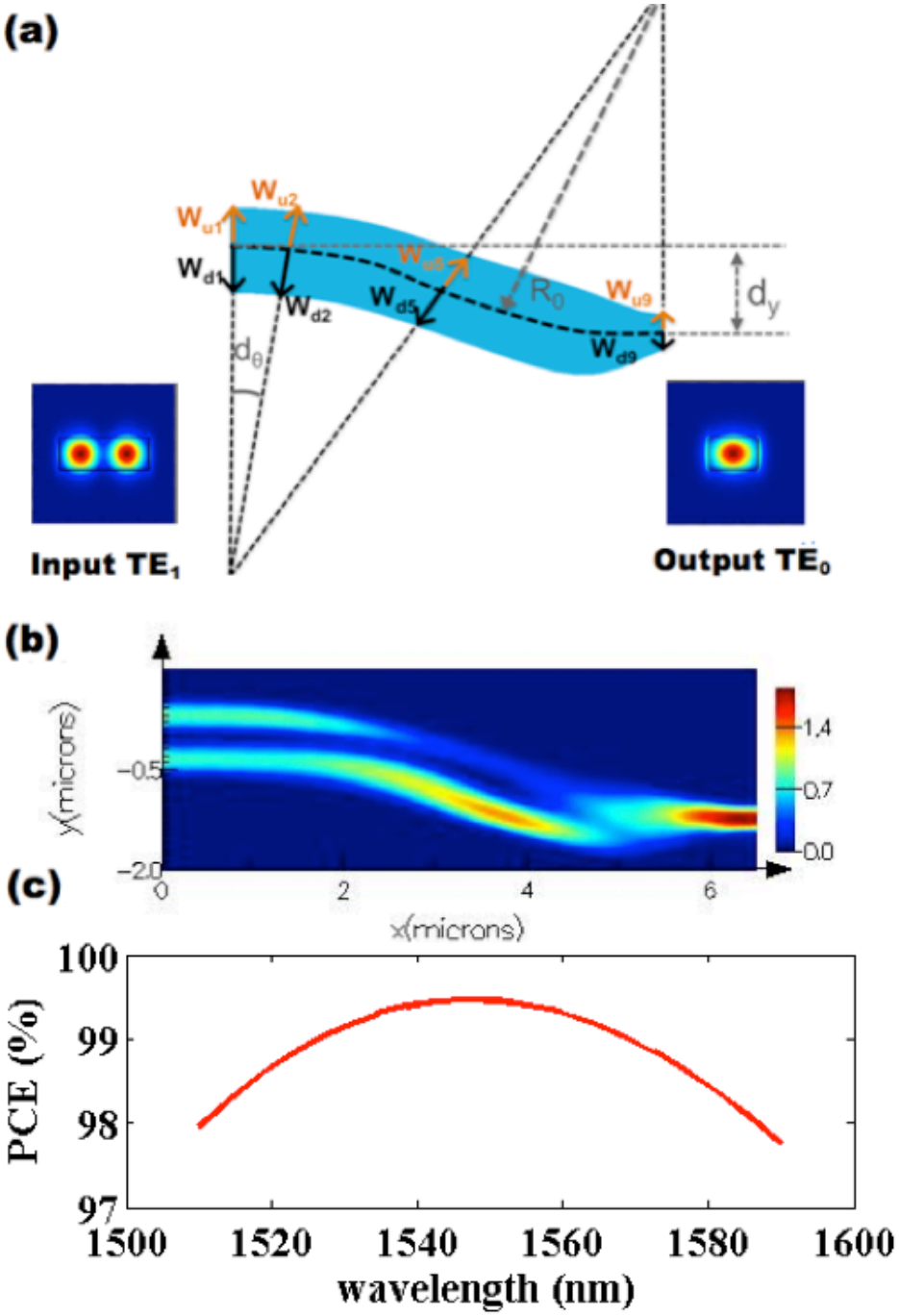

Figure 5.3. (a) Schematic of the bent-tapered TE_1-to-TE_0 mode converter (top view). (b) Simulated power distribution at 1550 nm wavelength. (c) Simulated PCE.

The TE1 mode is first launched into the left-hand port (width=1.25 μm). As seen in Figure 5.3(b), the two anti-phase components of TE_1 mode then travel with different effective lengths and eventually adiabatically combine to be the TE_0 mode at the right-hand side end (width=0.5 μm). During optimization, we found that there was no need to vary all the parameters. After several trials, we fixed the vertical offset dy to be 1.2 μm, and just optimized the center radius R_0 as well as the waveguide width sets. We found that near lossless conversion (99.5% efficiency, Figure 5.3(c)) can be achieved by optimizing the center radius and the last two segments (W_{u7}, W_{u8}, W_{d7}, W_{d8}), while other parameters were kept at their initial values. The first 6 segments were kept the same as the wide end, which has a width of 1.25 μm. After optimization, we found the optimum R_0=8.531 μm and the length of bent taper L=6.3 μm. The detailed geometric parameters are provided in Table II.

Table II. Converter width in nm

W_{u1}	W_{u2}	W_{u3}	W_{u4}	W_{u5}	W_{u6}	W_{u7}	W_{u8}	W_{u9}
625	625	625	625	625	625	616	426	250
W_{d1}	W_{d2}	W_{d3}	W_{d4}	W_{d5}	W_{d6}	W_{d7}	W_{d8}	W_{d9}
625	625	625	625	625	625	695	635	250

5.4 Performance of the complete polarization rotator

The behavior of this device, which was formed by the above two mode converters, was verified with 3-D FDTD simulation. Figure 5.4(a) shows the mode profile when launching the TM_0 mode at the left port. As we can see, the TM_0 mode first converts into the TE_1 mode when passing through the bi-level taper, and then converts into the TE_0 mode when passing though the bent-taper. Figure 5.4(b)

and 4(c) show the total polarization conversion loss and the extinction ratio of the proposed polarization rotator, respectively. The polarization rotator shows a less than 0.2 dB polarization conversion loss and a 25 dB extinction ratio. When launching the TE_0 mode into the input of the polarization rotator, significant power loss occurs due to scattering and almost all the remaining power (~ 40%) turns into the TE_1 mode and other higher order modes.

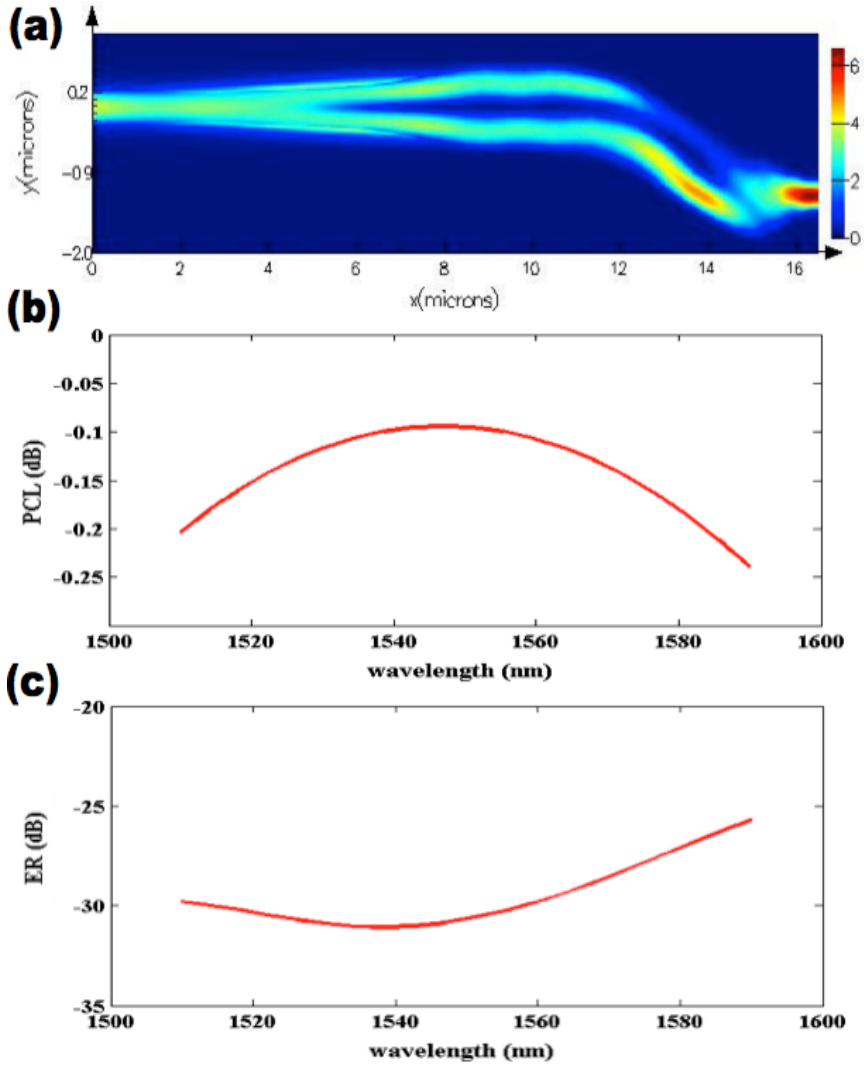

Figure 5.4. (a) Simulated power distribution at 1550 nm wavelength. The input TM_0 mode is launched from the left port, and the TE_0 mode comes out from the right port. (b) Simulated polarization conversion loss (PCL). (c) Simulated extinction ratio (ER) of the entire PR.

5.5 Fabrication tolerance analysis

To investigate the fabrication tolerance, three key geometry parameters (the height of partially-etched slab, the width of un-etched ridge waveguide, and the width of partially-etched slab) have been varied within +/- 40 nm. As shown in Figure 5.5, the polarization conversion loss does not experience any obvious degradation as the width of the un-etched ridge waveguide or the width of the partially-etched slab change. Thus, it is safe to conclude that the device has a high fabrication tolerance towards even +/- 40 nm width deviations. It is also evident that this device is relatively sensitive to the height of the partially-etched slab. But if we can control the height deviation of the partially-etched slab within +/- 10 nm (the actual height of the partially-etched slab ranges from 80 nm to 100 nm), the polarization conversion loss of the PR will not exceed 0.5 dB, which is quite decent. Overall, this device is fabrication insensitive and could be fabricated using optical lithography.

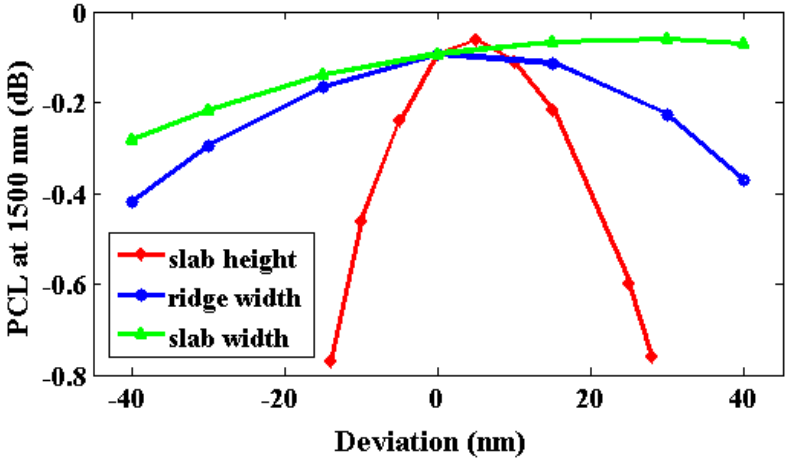

Figure 5.5. Simulated PCL at 1550 nm vs. fabrication deviation. The height of partially-etched slab is colored in red. The width of un-etched ridge waveguide is colored in blue. The width of the partially-etched slab is colored in green.

CHAPTER 6
SUMMARY, CONCLUSIONS AND OUTLOOK

In this thesis, various polarization-diversity devices have been proposed on a silicon-on-insulator platform. A polarization splitter-rotator based on a double-etched directional coupler was presented in Chapter 2. The proposed device has a very compact footprint and can be fabricated using a CMOS compatible process. In addition, a polarization splitter-rotator based on a bi-level mode converter and a Mach-Zehnder mode converter was shown in Chapter 3. To our best knowledge, this is the first polarization splitter-rotator working at O band on a silicon-on-insulator platform. The device was also patterned using a 248 nm deep ultra-violet lithography and potentially suitable for massive production. Furthermore, a bi-wavelength polarization splitter-rotator was proposed in Chapter 4. For a very long time, the on-chip bi-wavelength coupling could only be achieved using 2D grating couplers. Here, we demonstrated for the first time that it was possible to use polarization splitter-rotator combined with a wideband edge coupler to duplex light. Finally, in Chapter 5, we demonstrated an ultra-compact and high-efficiency polarization rotator, which was optimized by the particle swarm optimization method. To our best knowledge, this is the first time that evolutionary optimization method had been used to fully optimize the geometry of a polarization rotator. Furthermore, devices discussed in chapter 2 and 3 are still not ideal due to their fabrication sensitivities. We would suggest combining a directional coupler with a polarization rotator described in chapter 5 to achieve both high efficiency and robustness. These aforementioned works have been published [40-42] and have contributed significantly to further improving the

polarization transparency of silicon photonic circuits. This will enhance the viability of silicon photonics for commercialization.

In the future, we may want to send the bi-wavelength polarization splitter-rotator (demonstrated in Chapter 4) and the polarization rotator (demonstrated in Chapter 5) for fabrication and then experimentally verify their performance. Another effort that we plan to undertake is to integrate our polarization diversity devices with other silicon photonic devices to demonstrate some system-level designs, e.g. polarization-division multiplexing transceiver [113-114]. Besides that, it is also possible to demonstrate some hybrid multiplexing systems, e.g. WDM/PDM and MDM/PDM. Last but not least, we are also interested in exploring the possibility of using the polarization diversity devices in network-on-chip applications to address the challenges of creating hitless optical routers [115].

BIBLIOGRAPHY

[1] A. R. Mickelson, “Silicon photonics for on-chip interconnections," Custom Integrated Circuits Conference (CICC) 1(8), 19-21 (2011).

[2] D. A. B. Miller and H. M. Ozaktas, “Limit to the bit-rate capacity of electrical interconnects from the aspect ratio of the system architecture,” Special Issue on Parallel Computing with Optical Interconnects, J. Parallel and Distributed Computing 41, 42-52 (1997).

[3] A. Masaki, “Electrical resistance as a limiting factor for high-performance computer packaging,” IEEE Circuits and Devices Magazine 5, 22-26 (1989).

[4] Y. Hoskote, S. Vangal, A. Singh, N. Borkar, and S. Borkar, “A 5-GHz mesh interconnect for a teraflops processor,” IEEE Micro, 27(5), 51–61 (2007).

[5] Q. Xu, D. Fattal, and R. G. Beausoleil, ”Silicon microring resonators with 1.5 μm radius,” Opt. Express 16, 4309-4315 (2008).

[6] M. Cherchi, S. Ylinen, M. Harjanne, M. Kapulainen, and T. Aalto, "Dramatic size reduction of waveguide bends on a micron-scale silicon photonic platform," Opt. Express 21, 17814-17823 (2013).

[7] Q. Xu, B. Schmidt, S. Pradhan, and M. Lipson, ”Micrometre-scale silicon electro-optic modulator,” Nature 435, 325 (2005).

[8] W. M. J. Green, M. J. Rooks, L. Sekaric, and Y. A. Vlasov, ”Ultra-compact, low RF power, 10 Gb/s silicon Mach-Zehnder modulator,” Opt. Express 15, 17106-17113 (2007).

[9] Y. Vlasov, W.M.J. Green, and F. Xia, ”High-throughput silicon nanophotonic wavelength-insensitive switch for on-chip optical networks,” Nature Photonics 2, 242-246 (2008).

[10] A. Novack, M. Gould, Y. Yang, Z. Xuan, M. Streshinsky, Y. Liu, G. Capellini, A. E.-J. Lim, G.-Q. Lo, T. Baehr-Jones, and M. Hochberg, "Germanium photodetector with 60 GHz bandwidth using inductive gain peaking," Opt. Express 21, 28387-28393 (2013).

[11] Y. Zhang, S. Yang, A. E.-J. Lim, G.-Q. Lo, C. Galland, T. Baehr-Jones, and M. Hochberg, "A compact and low loss Y-junction for submicron silicon waveguide," Opt. Express 21, 1310-1316 (2013).

[12] Y. Ma, Y. Zhang, S. Yang, A. Novack, R. Ding, A. E.-J. Lim, G.-Q. Lo, T. Baehr-Jones, and M. Hochberg, "Ultralow loss single layer submicron silicon waveguide crossing for SOI optical interconnect," Opt. Express 21, 29374-29382 (2013).

[13] Y. Vlasov, W. M. J. Green, and F. Xia, ”High-throughput silicon nanophotonic wavelength-insensitive switch for on-chip optical networks,” Nature Photonics 2, 242-246 (2008).

[14] Q. Lai, W. Hunziker, and H. Melchior, ”Low-power compact 22 thermooptic silica-on-silicon waveguideswitch with fast response,” IEEE Photon. Technol. Lett. 10, 681-683 (1998).

[15]https://www.datacenterdynamics.com/focus/archive/2012/12/advancements-silicon-photonics-are-key-data-center-speed.

[16] A. Fang, H. Park, O. Cohen, R. Jones, M. Paniccia, and J. Bowers, ”Electrically pumped hybrid AlGaInAs-silicon evanescent laser,” Opt. Express 14, 9203-9210 (2006).

[17] M. Belt and D. J. Blumenthal, "Erbium-doped waveguide DBR and DFB laser arrays integrated within an ultra-low-loss Si3N4 platform," Opt. Express 22, 10655-10660 (2014).

[18] P. Boucaud, M. El Kurdi, A. Ghrib, M. Prost, M. de Kersauson, S. Sauvage, F. Aniel, X. Checoury, G. Beaudoin, L. Largeau, I. Sagnes, G. Ndong, M. Chaigneau, and R. Ossikovski, "Recent advances in germanium emission [Invited]," Photon. Res. 1, 102-109 (2013).

[19] M. Streshinsky, R. Ding, Y. Liu, A. Novack, Y. Yang, Y. Ma, X. Tu, E. K. Sing Chee, A. E.-J. Lim, P. G.-Q. Lo, T. Baehr-Jones, and M. Hochberg, "Low power 50 Gb/s silicon traveling wave Mach-Zehnder modulator near 1300 nm," Opt. Express 21, 30350-30357 (2013).

[20] J. C. Rosenberg, W. M. J. Green, S. Assefa, D. M. Gill, T. Barwicz, M. Yang, S. M. Shank, and Y. A. Vlasov, "A 25 Gbps silicon microring modulator based on an interleaved junction," Opt. Express 20, 26411-26423 (2012).

[21] C. T. DeRose, D. C. Trotter, W. A. Zortman, A. L. Starbuck, M. Fisher, M. R. Watts, and P. S. Davids, "Ultra compact 45 GHz CMOS compatible Germanium waveguide photodiode with low dark current," Opt. Express 19, 24897-24904 (2011).

[22] S. Zhu, M. B. Yu, G. Q. Lo, and D. L. Kwong, ”Near-infrared waveguidebased nickel silicide Schottky-barrier photodetector for optical communications,” Appl. Phys. Lett. 92, 081103 (2008).

[23] H. Park, A. W. Fang, R. Jones, O. Cohen, O. Raday, M. Sysak, M. Paniccia, and J. Bowers, "A hybrid AlGaInAs-silicon evanescent waveguide photodetector," Opt. Express 15, 6044-6052 (2007).

[24] N. Sherwood-Droz, H. Wang, L. Chen, B. G. Lee, A. Biberman, K. Bergman, and M. Lipson, "Optical 4x4 hitless slicon router for optical networks-on-chip (NoC)," Opt. Express 16, 15915-15922 (2008).

[25] W. D. Sacher, T. Barwicz, B. J. F. Taylor, and J. K. S. Poon, "Polarization rotator-splitters in standard active silicon photonics platforms," Opt. Express 22, 3777-3786 (2014).

[26] W. Bogaerts, P. Dumon, D. V. Thourhout, and R. Baets, "Low-loss, low-cross-talk crossings for silicon-on-insulator nanophotonic waveguides," Opt. Lett. 32, 2801-2803 (2007).

[27] M. Hochberg, N. Harris, R. Ding, Y. Zhang, A. Novack, Z. Xuan, and T. Baehr-Jones, "Silicon photonics: the next fabless semiconductor industry," IEEE Solid-State Circuits Magazine5, 48–58 (2013).

[28] http://www.helios-project.eu/

[29] http://www.rle.mit.edu/isg/On-ChipIntegratedCMOSPhotonics.htm

[30] http://www.luxtera.com/

[31] D. Dai, L. Liu, L. Wosinski, and S. He, "Design and fabrication of ultra-small overlapped AWG demultiplexer based on Si nanowire waveguides," Electron. Lett. 42(7), 400–402 (2006).

[32] D. Dai, L. Liu, S. Gao, D. X. Xu, and S. He, "Polarization management for silicon photonic integrated circuits," Laser Photon. Rev. 7, 303–328 (2013).

[33] T. Barwicz, M. R. Watts, M. A. Popovic, P. T. Rakich, L. Socci, F. X. Kartner, E. P. Ippen, and H. I. Smith, “Polarization Transparent Microphotonic Devices in the Strong Confinement Limit,” Nat. Photonics 1(1), 57-60 (2007).

[34] D. Dai, "Ultracompact polarization diversity components for future large-scale photonic integrated circuits on silicon," Proc. SPIE 8629, Silicon Photonics VIII, 86290B (2013).

[35] D. Dai, "Silicon mode-(de)multiplexer for a hybrid multiplexing system to achieve ultrahigh capacity photonic networks-on-chip with a single wavelength-carrier light," in Asia Communications and Photonics Conference, OSA Technical Digest (online) (Optical Society of America, 2012), paper ATh3B.3.

[36] L.-W. Luo, N. Ophir, C. P. Chen, L. Gabrielli, C. B. Poitras, K. Bergman, and M. Lipson,” WDM-compatible mode-division multiplexing on a silicon chip," Nat. Comm., 5, 3069, (2014).

[37] T. Pfau, R. Peveling, J. Hauden, N. H. Porte, Y. Achiam, S. Hoffmann, S. K. Ibrahim, O. Adamczyk, S. Bhandare, D. Sandel, M. Porrmann, and R. Noé, “Coherent digital polarization diversity receiver for real-time polarization-multiplexed QPSK transmission at 2.8 Gb/s,” IEEE Photon. Technol. Lett. 19, 1988-1990 (2007).

[38] L. Sansoni, F. Sciarrino, G. Vallone, P. Mataloni, A. Crespi, R. Ramponi, and R. Osellame “Polarization Entangled State Measurement on a Chip,” Phys. Rev. Lett. 105, 200503 (2010).

[39] http://opsisfoundry.org/

[40] H. Guan, A. Novack, M. Streshinsky, R. Shi, Q. Fang, A. E.-J. Lim, G.-Q. Lo, T. Baehr-Jones, and M. Hochberg, "CMOS-compatible highly efficient polarization splitter and rotator based on a double-etched directional coupler," Opt. Express 22, 2489-2496 (2014)

[41] H. Guan, A. Novack, M. Streshinsky, R. Shi, Y. Liu, Q. Fang, A.E. Lim, G. Lo, T. Baehr-Jones, and M. Hochberg," High-efficiency low-crosstalk 1310-nm polarization splitter and rotator built on a SOI platform," IEEE Photon. Technol. Lett. 26(9), 925-928 (2014).

[42] H. Guan, Y. Ma, R. Shi, A. Novack, J. Tao, Q. Fang, A. E. Lim, G. Lo, T. Baehr-Jones, and M. Hochberg," Ultra-compact silicon-on-insulator polarization rotator for polarization-diversified circuits," Opt. Lett. (In press).

[43] T. Baehr-Jones, T. Pinguet, P. G.-Q. Lo, S. Danziger, D. Prather, and M. Hochberg, “Myths and rumours of silicon photonics,” Nat. Photonics 6(4), 206–208 (2012).

[44] M. Hochberg and T. Baehr-Jones, "Towards fabless silicon photonics,” Nat. Photonics 4(8), 492–494 (2010).

[45] F. Xia, L. Sekaric, and Y. Vlasov, “Ultracompact optical buffers on a silicon chip,” Nat. Photonics 1(1), 65–71 (2007).

[46] D. Dai and J. E. Bowers, "Novel concept for ultracompact polarization splitter-rotator based on silicon nanowires," Opt. Express 19(11), 10940-10949 (2011).

[47] T. Barwicz, M. R. Watts, M. A. Popovic, P. T. Rakich, L. Socci, F. X. Kartner, E. P. Ippen, and H. I. Smith, “Polarization Transparent Microphotonic Devices in the Strong Confinement Limit,” Nat. Photonics 1(1), 57-60 (2007).

[48] H. Fukuda, K. Yamada, T. Tsuchizawa, T. Watanabe, H. Shinojima, and S. I. Itabashi, “Silicon photonic circuit with polarization diversity,” Opt. Express 16(7), 4872-4880 (2008).

[49] J. Zhang, H. Zhang, S. Chen, M. Yu, G. Q. Lo, and D. L. Kwong, “A tunable polarization diversity silicon photonics filter,” Opt. Express 19(14), 13063–13072 (2011).

[50] Y. Ding, L. Liu, C. Peucheret, and H. Ou, "Fabrication tolerant polarization splitter and rotator based on a tapered directional coupler," Opt. Express 20(18), 20021-20027 (2012).

[51] W. Bogaerts, D. Taillaert, P. Dumon, D. Van Thourhout, R. Baets, and E. Pluk, “A polarization-diversity wavelength duplexer circuit in silicon-on-insulator photonic wires,” Opt. Express 15(4), 1567–1578 (2007).

[52] L. Chen, C.R. Doerr, Y.-K. Chen, and T.-Y. Liow, "Low-Loss and Broadband Cantilever Couplers Between Standard Cleaved Fibers and High-Index-Contrast Si3N4 or Si Waveguides," IEEE Photon. Technol. Lett. 22(23), 1744-1746 (2010).

[53] L. Chen, C. R. Doerr, and Y.-K. Chen, "Compact polarization rotator on silicon for polarization-diversified circuits," Opt. Lett. 36(4), 469-471 (2011).

[54] Y. Fei, L. Zhang, T. Cao, Y. Cao, and S. Chen, "High Efficiency Broadband Polarization Converter Based on Tapered Slot Waveguide," IEEE Photon. Technol. Lett. 25(9), 879-881 (2013).

[55] L. Liu, Y. Ding, K. Yvind, and J. M. Hvam, "Silicon-on-insulator polarization splitting and rotating device for polarization diversity circuits," Opt. Express 19(13), 12646-12651 (2011).

[56] D. Vermeulen, S. Selvaraja, P. Verheyen, P. Absil, W. Bogaerts, D. Van Thourhout, and G. Roelkens, "Silicon-on-Insulator Polarization Rotator Based on a Symmetry Breaking Silicon Overlay," IEEE Photon. Technol. Lett. 24(6), 879-881 (2012).

[57] M. Aamer, A. M. Gutierrez, A. Brimont, D. Vermeulen, G. Roelkens, J.-M. Fedeli, A. Hakansson, and P. Sanchis, "CMOS Compatible Silicon-on-Insulator Polarization Rotator Based on Symmetry Breaking of the Waveguide Cross Section," IEEE Photon. Technol. Lett. 24(22), 2031-2034 (2012).

[58] Z. Wang and D. Dai, "Ultrasmall Si-nanowire-based polarization rotator," J. Opt. Soc. Am. B 25(5), 747-753 (2008).

[59] X. Xiong, C.-L. Zou, X.-F. Ren, and G.-C. Guo, "Integrated polarization rotator/converter by stimulated Raman adiabatic passage," Opt. Express 21(14), 17097-17107 (2013).

[60] A. Mekis, S. Gloeckner, G. Masini, A. Narasimha, T. Pinguet, S. Sahni, and P. De Dobbelaere, "A Grating-Coupler-Enabled CMOS Photonics Platform," IEEE J Sel. Top. Quantum Electron. 17(3), 597-608 (2011).

[61] D. Dai, J. Bauters, and J. E. Bowers, “Passive technologies for future large-scale photonic integrated circuits on silicon: polarization handling, light non-reciprocity and loss reduction,” Light: Sci. Appl. 1(3), 1–14 (2012).

[62] L. B. Soldano, A. H. de Vreede, M. K. Smit, B. H. Verbeek, E. G. Metaal, and F. H. Groen, “Mach-Zehnder interferometer polarization splitter in InGaAsP-InP,” IEEE Photon. Technol. Lett. 6(3), 402–405 (1994).

[63] T. K. Liang and H. K. Tsang, “Integrated PBS in high index contrast silicon-on-insulator waveguides,” IEEE Photon. Technol. Lett. 17(2), 393–395 (2005).

[64] L. M. Augustin, R. Hanfoug, J. J. G. M. van der Tol, W. J. M. de Laat, and M. K. Smit, “A compact integrated polarization splitter/converter in InGaAsP-InP,” IEEE Photon. Technol. Lett. 19(17), 1286–1288 (2007).

[65] D. Dai, Z. Wang, and J. E. Bowers, “Considerations for the design of asymmetrical Mach-Zehnder Interferometers used as polarization beam splitters on a sub-micron silicon-on-insulator platform,” J. Lightwave Technol. 29(12), 1808–1817 (2011).

[66] J. M. Hong, H. H. Ryu, S. R. Park, J. W. Jeong, S. G. Lee, E. H. Lee, S. G. Park, D. Woo, S. Kim, and B. H. O,“Design and fabrication of a significantly shortened multimode interference coupler for polarization splitter application,” IEEE Photon. Technol. Lett. 15(1), 72–74 (2003).

[67] B. K. Yang, S. Y. Shin, and D. M. Zhang, “Ultrashort polarization splitter using two-mode interference in silicon photonic wires,” IEEE Photon. Technol. Lett. 21(7), 432–434 (2009).

[68] I. Kiyat, A. Aydinli, and N. Dagli, “A compact silicon-on-insulator polarization splitter,” IEEE Photon. Technol.Lett. 17(1), 100–102 (2005).

[69] X. G. Tu, S. S. N. Ang, A. B. Chew, J. Teng, and T. Mei, “An ultracompact directional coupler based on GaAs cross-slot waveguide,” IEEE Photon. Technol. Lett. 22(17), 1324–1326 (2010).

[70] T. Yamazaki, H. Aono, J. Yamauchi, and H. Nakano, “Coupled waveguide polarization splitter with slightly different core widths,” J. Lightwave Technol. 26(21), 3528–3533 (2008).

[71] Y. Shi, D. Dai, and S. He, “Proposal for an ultra-compact PBS based on a photonic crystal-assisted multimode interference coupler,” IEEE Photon. Technol. Lett. 19(11), 825–827 (2007).

[72] X. Ao, L. Liu, W. Lech, and S. He, “Polarization beam splitter based on a two-dimensional photonic crystal of pillar type,” Appl. Phys. Lett. 89(17), 171115 (2006).

[73] X. Xiong, C. -L. Zou, X. -F Ren, and G. –C. Guo, "Integrated polarization rotator/converter by stimulated Raman adiabatic passage," Opt. Express 21(14), 17097-17107 (2013).

[74] Y. Wakabayashi, T. Hashimoto, J. Yamauchi, H. Nakano, "Short Waveguide Polarization Converter Operating Over a Wide Wavelength Range," J. Lightwave Technol. 31(10), 1544-1550 (2013).

[75] M. Aamer, A. M. Gutierrez, A. Brimont, D. Vermeulen, G. Roelkens, J.-M. Fedeli, A. Hakansson, P. Sanchis, "CMOS Compatible Silicon-on-Insulator Polarization Rotator Based on Symmetry Breaking of the Waveguide Cross Section," IEEE Photon. Technol. Lett. 24(22), 031-2034 (2012).

[76] J. Wang and D. Dai, "Ultra-small silicon polarization beam splitter based on cascaded asymmetry directional couplers," in Proc. Conf. Opt. Fiber Commun., paper OTh4I.1.

[77] D. Dai and J. E. Bowers, "Novel concept for ultracompact polarization splitter-rotator based on silicon nanowires," Opt. Express 19(11), 10940-10949 (2011).

[78] W. Yuan, K. Kojima, B. Wang, T. Koike-Akino, K. Parsons, S. Nishikawa, and E. Yagyu, "Mode-evolution-based polarization rotator-splitter design via simple fabrication process," Opt. Express 20(9), 10163-10169 (2012).

[79] M. Komatsu, K. Saitoh, and M. Koshiba, “Compact polarization rotator based on surface plasmon polariton with low insertion loss,” J. Photon. 4(3), 707-714 (2012).

[80] J. N. Caspers, M. Z. Alam, and M. Mojahedi, “Compact hybrid plasmonic polarization rotator,” Opt. Lett. 37(22), 4615–4617 (2012).

[81] L. Chen, C. R. Doerr, and Y. K. Chen, “Compact polarization rotator on silicon for polarization-diversified circuits,” Opt. Lett. 36(4), 469–471 (2011).

[82] H. Fukuda, K. Yamada, T. Tsuchizawa, T. Watanabe, H. Shinojima, and S. I. Itabashi, “Silicon photonic circuit with polarization diversity,” Opt. Express 16(7), 4872-4880 (2008).

[83] H. Fukuda, K. Yamada, T. Tsuchizawa, T. Watanabe, H. Shinojima, and S. I. Itabashi, "Ultrasmall polarization splitter based on silicon wire waveguides," Opt. Express 14(25), 12401-12408 (2006).

[84] D. Dai, Y. Tang, and J. E. Bowers, "Mode conversion in tapered submicron silicon ridge optical waveguides," Opt. Express 20(12), 13425–13439 (2012).

[85] Y. Huang, G. Xu, and S.-T. Xu, “An ultracompact optical mode order converter,” IEEE Photon. Technol. Lett. 18(21), 2281-2283 (2006).

[86] A. Banerjee, Y. Park, F. Clarke, H. Song, S. Yang, G. Kramer, K. Kim, and B. Mukherjee, "Wavelength-division-multiplexed passive optical network (WDM-PON) technologies for broadband access: a review [Invited]," J. Opt. Netw. 4(11), 737-758 (2005).

[87] G. Roelkens, D. Vermeulen, S. Selvaraja, R. Halir, W. Bogaerts, and D. Van Thourhout, “Grating-based optical fiber interfaces for silicon-on-insulator photonic integrated circuits,” IEEE J. Sel. Top. Quantum Electron. 17(3), 571–580 (2011).

[88] L. Xu, X. Chen, C. Li, and H. K. Tsang, “Bi-wavelength two dimensional chirped grating couplers for low cost WDM PON transceivers,” Opt. Commun. 284(8), 2242–2244 (2011).

[89] W. Bogaerts, D. Taillaert, P. Dumon, E. Pluk, D. Van Thourhout, and R. Baets, “A compact polarization independent wavelength duplexer using a polarization-diversity SOI photonic wire circuit,” in Optical Fiber Communication and National Fiber Optic Engineers Conference (Optical Society of America, Anaheim, California, 2007), pp. 1–3.

[90] M. Streshinsky, R. Shi, A. Novack, R. T. P. Cher, A. E.-J. Lim, P. G.-Q. Lo, T. Baehr-Jones, and M. Hochberg, "A compact bi-wavelength polarization splitting grating coupler fabricated in a 220 nm SOI platform," Opt. Express 21(25), 31019-31028 (2013).

[91] B. B. Bakir, A. V. Gyves, R. Orobtchouk, P. Lyan, C. Porzier, A. Roman, and J. M. Fedeli, “Low-loss (<1dB) and polarization-insensitive edge fiber couplers fabricated on 200-mm silicon-on-insulator wafers,” IEEE Photon. Technol. Lett. 22(11), 739–741 (2010).

[92] Q. Fang, J. Song, X. Luo, M. Yu, G. Lo, and Y. Liu, "Mode-size converter with high coupling efficiency and broad bandwidth," Opt. Express 19(22), 21588-21594 (2011).

[93] J. Wang, B. Niu, Z. Sheng, A. Wu, X. Wang, S. Zou, M. Qi, and F. Gan, "Design of a SiO2 top-cladding and compact polarization splitter-rotator based on a rib directional coupler," Opt. Express 22(4), 4137-4143 (2014).

[94] Y. Ding, H. Ou, and C. Peucheret, "Wideband polarization splitter and rotator with large fabrication tolerance and simple fabrication process," Opt. Lett. 38(8), 1227-1229 (2013).

[95] W. D. Sacher, T. Barwicz, B. J. F. Taylor, and J. K. S. Poon, "Polarization rotator-splitters in standard active silicon photonics platforms," Opt. Express 22(4), 3777-3786 (2014).

[96] C. Alonso-Ramos, S. Romero-García, A. Ortega-Moñux, I. Molina-Fernández, R. Zhang, H. G. Bach, and M. Schell, "Polarization rotator for InP rib waveguide," Opt. Lett. 37, 335-337 (2012).

[97] M. Kotlyar, L. Bolla, M. Midrio, L. O'Faolain, and T. Krauss, "Compact polarization converter in InP-based material," Opt. Express 13, 5040-5045 (2005).

[98] K. Bayat, S. K. Chaudhuri, and S. Safavi-Naeini, "Ultra-compact photonic crystal based polarization rotator," Opt. Express 17, 7145-7158 (2009).

[99] L. Sánchez and P. Sanchis, "Broadband 8 μm long hybrid silicon-plasmonic transverse magnetic–transverse electric converter with losses below 2 dB," Opt. Lett. 38(15), 2842-2845 (2013).

[100] J. N. Caspers, J. S. Aitchison, and M. Mojahedi, "Experimental demonstration of an integrated hybrid plasmonic polarization rotator," Opt. Lett. 38(20), 4054-4057 (2013).

[101] L. Jin, Q. Chen, and L. Wen, "Mode-coupling polarization rotator based on plasmonic waveguide," Opt. Lett. 39(9), 2798-2801 (2014).

[102] G. Chen, L. Chen, W. Ding, F. Sun, and R. Feng, "Ultra-short Silicon-On-Insulator (SOI) polarization rotator between a slot and a strip waveguide based on a nonlinear raised cosine flat-tip taper," Opt. Express 21, 14888-14894 (2013).

[103] G. Chen, L. Chen, W. Ding, F. Sun, and R. Feng, "Ultrashort slot polarization rotator with double paralleled nonlinear geometry slot crossings," Opt. Lett. 38, 1984-1986 (2013).

[104] M. R. Watts and H. A. Haus, "Integrated mode-evolution-based polarization rotators," Opt. Lett. 30, 138-140 (2005).

[105] P. Sanchis, P. Villalba, F. Cuesta, A. Håkansson, A. Griol, J. V. Galán, A. Brimont, and J. Martí, "Highly efficient crossing structure for silicon-on-insulator waveguides," Opt. Lett. 34(18), 2760–2762 (2009).

[106] J. Kennedy and R. Eberhart, "Particle swarm optimization," Proc. IEEE Intern. Conf. Neural Networks (1995).

[107] J. Robinson and Y. Rahmat-Samii, "Particle swarm optimization in electromagnectis," IEEE Trans. Antenn. Propag. 52(2), 397–407 (2004).

[108] M. Shokooh-Saremi and R. Magnusson, "Particle swarm optimization and its application to the design of diffraction grating filters," Opt. Lett. 32, 894-896 (2007).

[109] S. Baskar, R.T. Zheng, A. Alphones, N.Q. Ngo, and P.N. Suganthan, "Particle swarm optimization for the design of low-dispersion fiber Bragg gratings," IEEE Photon. Technol. Lett. 17(3), 615-617 (2005).

[110] https://www.lumerical.com/tcad-products/fdtd/features/

[111] D. Dai, J. Wang, and Y. Shi, "Silicon mode (de)multiplexer enabling high capacity photonic networks-on-chip with a single-wavelength-carrier light," Opt. Lett. 38(9), 1422-1424 (2013).

[112] Y. Ding, J. Xu, F. D. Ros, B. Huang, H. Ou, and C. Peucheret, "On-chip two-mode division multiplexing using tapered directional coupler-based mode multiplexer and demultiplexer," Opt. Express 21(8), 10376-10382 (2013).

[113] P. Dong, C. Xie, L. Chen, L. L. Buhl, and Y.-K. Chen, "112-Gb/s monolithic PDM-QPSK modulator in silicon," Opt. Express 20, B624-B629 (2012).

[114] P. Dong, L. Chen, C. Xie, L. L. Buhl, and Y.-K. Chen, "50-Gb/s silicon quadrature phase-shift keying modulator," Opt. Express 20, 21181-21186 (2012).

[115] N. Sherwood-Droz, H. Wang, L. Chen, B. G. Lee, A. Biberman, K. Bergman, and M. Lipson, "Optical 4x4 hitless slicon router for optical networks-on-chip (NoC)," Opt. Express 16, 15915-15922 (2008).

LIST OF PUBLICATIONS

Journal publications

[1] H. Guan, A. Novack, M. Streshinsky, R. Shi, Q. Fang, A. E.-J. Lim, G.-Q. Lo, T. Baehr-Jones, and M. Hochberg, "CMOS-compatible highly efficient polarization splitter and rotator based on a double-etched directional coupler," Opt. Express 22, 2489-2496 (2014).

[2] H. Guan, A. Novack, M. Streshinsky, R. Shi, Y. Liu, Q. Fang, A. E.-J. Lim, G.-Q. Lo, T. Baehr-Jones, and M. Hochberg, "High efficiency, low crosstalk 1310 nm polarization splitter and rotator built on a silicon-on-insulator platform," IEEE Photon. Technol. Lett. 26, 925-928 (2014).

[3] H. Guan, Y. Ma, R. Shi, A. Novack, J. Tao, . Fang, A. E.-J. Lim, G.-Q. Lo, T. Baehr-Jones, and M. Hochberg, “Ultra-compact silicon-on-insulator polarization rotator for polarization-diversified circuits”, Opt. Lett. (in press).

[4] H. Guan, A. Novack, M. Streshinsky, R. Shi, Y. Liu, Q. Fang, A. E.-J. Lim, G.-Q. Lo, T. Baehr-Jones, and M. Hochberg, “A highly efficient bi-wavelength polarization splitter and rotator”, Opt. Express (under review).

[5] R. Shi, H. Guan, A. Novack, M. Streshinsky, A. E.-J. Lim, G.-Q. Lo, T. Baehr-Jones, and M. Hochberg, “High-Efficiency Grating Coupler near 1310 nm Fabricated by 248 nm DUV Lithography”, IEEE Photon. Technol. Lett. 99, 1-4 (2014).

[6] Y. Zhang, S. Yang, H. Guan, A. E.-J. Lim, G.-Q. Lo, P. Magill, T. Baehr-Jones, and M. Hochberg, “Sagnac loop mirror and micro-ring based laser cavity for silicon-on-insulator”, Opt. Express (in press).